Supplementary Information

Anion-Decoupled Electrolytes Enable Stable Cycling and Fast Interfacial Kinetics for Calcium Metal Anodes

*Qi Meng, Zhen Zhan, Yiyuan Ma, Qi Qi, Yingkai Hua, Yuyang Yi, Jingya Yu, Mengcheng Wu, Jingjing Tang, Songhua Cai, Kang Cheung Chan, Zheng-Long Xu**

Qi Meng, Yiyuan Ma, Qi Qi, Yingkai Hua, Yuyang Yi, Jingya Yu, Mengcheng Wu, Kang Cheung Chan, Zheng-Long Xu
Department of Industrial and Systems Engineering, The Hong Kong Polytechnic University, Hung Hom, Hong Kong SAR, China.
E-mail: zhenglong.xu@polyu.edu.hk

Zhen Zhan, Prof. Songhua Cai
Department of Applied Physics, The Hong Kong Polytechnic University, Hung Hom, Hong Kong, China.

Kang Cheung Chan, Zheng-Long Xu
State Key Laboratory of Ultra-precision Machining Technology, Research Institute of Advanced Manufacturing, The Hong Kong Polytechnic University, Hung Hom, Hong Kong SAR, China.

Prof. Zheng-Long Xu
Shenzhen Research Institute, The Hong Kong Polytechnic University, Shenzhen, China

Jingjing Tang
School of Metallurgy and Environment, Central South University, Changsha, China.

Experimental Section

Preparation of electrolytes: The dimethoxyethane (G1, Sigma-Aldrich, 99.5%), diethylene glycol dimethyl ether (G2, Sigma-Aldrich, 99.5%), tetraethylene glycol dimethyl ether (G4, Sigma-Aldrich, ≥99%), ethylene carbonate/propylene carbonate (EC/PC, 1:1 Vol%, DoDoChem, 99.95%), 1,3-Dioxolane (DOL, Sigma-Aldrich, 99.8%), dimethyl sulfoxide (DMSO, Sigma-Aldrich, ≥99.9%), dimethylformamide (DMF, TCI, 99.5%), tetrahydrofuran (THF, ≥99.9%, Aladdin), dimethylacetamide (DMAc, Sigma-Aldrich, ≥99.9%) solvents were dried by molecular sieves for 24 hours before use. Electrolytes were prepared by dissolving 0.3 M $Ca(TFSI)_2$ (99.0%, DoDoChem) in these solvents. The 1,2-dibromobenzene (1,2-DBB, >97%, TCI) was added into the DMAc electrolyte at various volume fractions, with 0.5 vol% identified as the optimal ratio. 1,2-difluorobenzene (1,2-DFB, >98%, TCI), 1,2-dichlorobenzene (1,2-DCB, >99%, TCI), 1- Bromobenzene (1-BB) (>99.0%, TCI) were added into the DMAc electrolyte at 0.5 vol%. 1,3,5-Tribromobenzene (1,3,5-TBB) (>98.0%, TCI) was added into the DMAc electrolyte at 0.5 wt% because of its solid phase at room temperature.

Materials characterization: Raman spectroscopy was conducted on the Renishaw Micro-Raman Spectroscopy System with an excitation wavelength of 532 nm. FTIR spectra of the functional groups in 9,10-phenanthrenequinone (PQ) were recorded on a Bruker spectrometer equipped with a Pike MIRacle single-bounce attenuated total reflectance accessory (ATR, ZnSe IRE). Nuclear magnetic resonance (NMR) spectra were collected on Bruker Avance NEO 400MHz NMR spectrometer. The X-ray Photoelectron Spectroscopy (XPS) depth profiling was performed on Thermo Scientific spectrometer equipped with an Al-Kα X-ray source (1486.6 eV). Sputter etching was carried out with a 2 kV Ar^+ ion beam. Time-of-flight secondary ion mass spectrometry (TOF-SIMS) was performed using a PHI nanoTOF II instrument with a Bi^{3+} gun at 30 keV and an Ar^+ sputtering beam working at 3 KV and 100 nA. XPS and TOF-SIMS samples were transferred into the chamber under an inert atmosphere without exposure to air. The X-ray diffraction patterns were collected on Rigaku SmartLab 9 kW X-ray diffractometer (Cu Kα radiation, λ = 1.5418 Å, current: 20 mA, voltage: 45 kV) in a scan range (2θ) of 10°-60°. The morphology and energy dispersive X-ray spectroscopy (EDS) mapping of the materials were collected on scanning electron microscopy (SEM, TESCAN MIRA). The high-resolution transmission electron microscopy (HRTEM) images were captured under a Cs-corrected STEM (Thermo Scientificrm Spectra300 S/TEM) operated at 300 kV.

Electrochemical measurements: CR2032 coin cells were assembled in an argon-filled glove box using glass fiber separators. The Ca foils (diameter: 10 mm, thickness: 500 μm) were polished to shiny surface before using. Electrochemical tests of coin cells were carried out on

Neware battery testers. Electrochemical impedance spectroscopy (EIS) measurement was performed on the BioLogic VSP-3e electrochemical workstation from 1 MHz and 10 mHz under a potential amplitude of 5 mV. The cell was cycled for 5, 10, 15 and 20 cycles at 0.1 mA cm^{-2} and 0.1 mAh cm^{-2} and rested to equilibrium for EIS measurements. Ionic conductivities were measured by EIS tests using the blocking electrode (stainless steel, SS). Cyclic voltammetry (CV) tests of Ca//Ca symmetric cells and Ca//carbon paper (CC) cells were carried out on the BioLogic VSP-3e electrochemical workstation at a scan rate of 20 mV s^{-1}.

For Ca//graphite cells, graphite electrodes were prepared by mixing graphite, super P, and polyvinylidene fluoride (PVDF, DoDoChem) with a weight ratio of 6: 3: 1 in N-methyl-2-pyrrolidone (NMP, DoDoChem) solvent and then cast onto aluminum foil. The electrode was dried overnight at 80 °C in a vacuum oven, and active material loading is ~ 1.1 mg cm^{-2}.

For Ca// PQ full cells, PQ cathodes were prepared by mixing PQ powder (purchased from TCI), single-walled carbon nanotubes, and polytetrafluoroethylene in a weight ratio of 6:3:1 and then pressed on the titanium mesh current collectors for electrochemical experiments after drying at 80 °C in a vacuum oven. The mass loading of PQ cathodes (Φ = 8 mm) is ~ 0.95 mg cm^{-2}.

Molecular dynamics (MD) simulations: MD simulations were conducted in the Forcite module in Materials studio 2020. All dynamic simulations employed the COMPASS III force field. The electrolyte systems underwent simulated annealing between 600 K and 300 K using the NTV ensemble for 25 cycles, with the structure optimized after each annealing cycle. The structure with the lowest energy was selected for the subsequent MD simulations. The electrolyte systems were equilibrated under NPT ensemble using the Berendsen barostat to maintain a pressure of 0.0001 GPa for 1000 ps, ensuring that the system achieved the appropriate density. After equilibration, the system was simulated for 1000 ps under the NVT ensemble at 298 K, with the last 500 ps of the trajectory used for analyzing the Ca^{2+} coordination environment.

Density functional theory (DFT) calculations: All quantum chemistry calculations were performed using Gaussian 16 software. The geometry optimization and frequency calculation were performed using the B3LYP exchange-correlation functional in conjunction with the basis set of 6-311+G(d, p) accompanied by the continuum solvation model based on the charge density (SMD, solvent = DMAc). All the optimized structures were confirmed as potential minima, no frequency modes with imaginary eigenvalues, through frequency analyses following geometry optimizations. The binding energies (E_{bind}) of different complexes were calculated according to the formula:

$$E_{bind} = E_{complex}\text{-}E_A\text{-}E_B$$

Where $E_{complex}$ is the total energy of the binding complex, E_A (E_B) represents the energy of free metal ions, solvents and $TFSI^-$ anion. The analysis of the molecular orbitals, electrostatic potential (ESP), Mayer bond order and interaction region indicator (IRI)[1] were obtained from Multiwfn program[2-3], with visualization carried out using VMD.

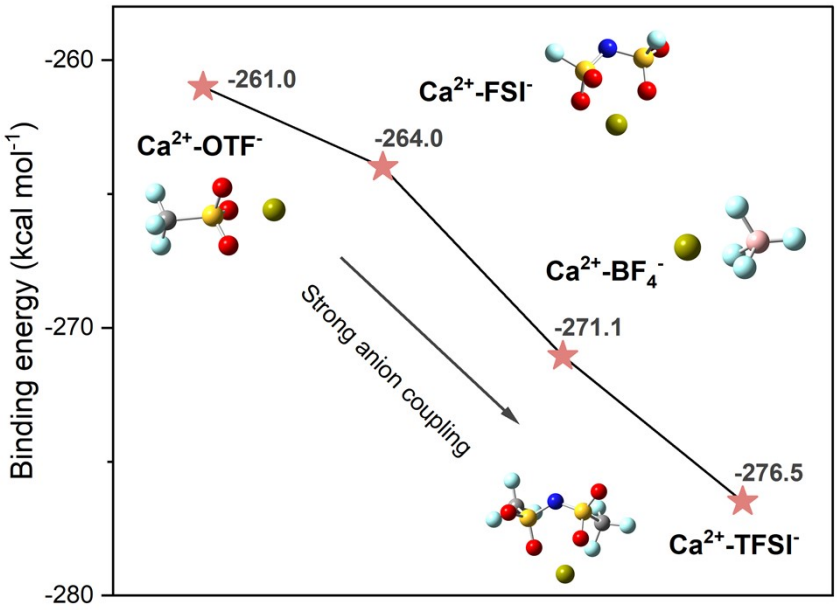

Figure S1. Binding energies between Ca^{2+} and OTF^-, FSI^-, BF_4^- and $TFSI^-$ anions.

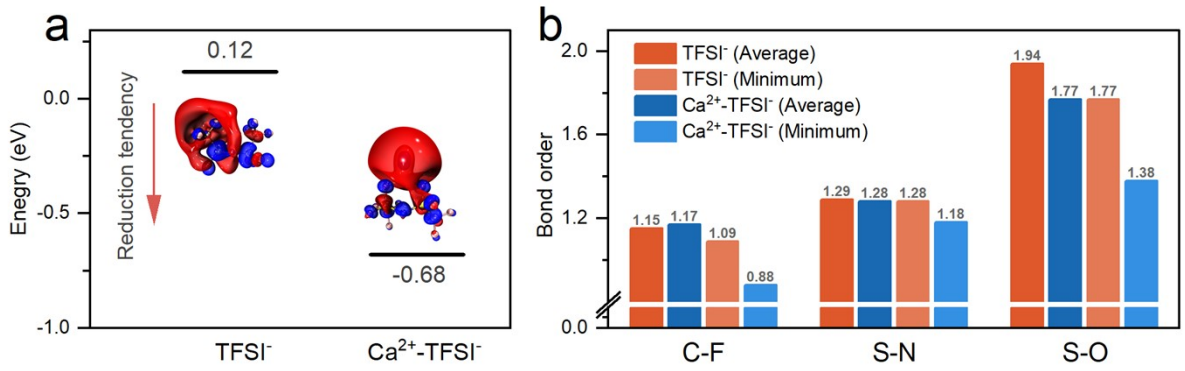

Figure S2. (a) LUMO energies of free $TFSI^-$ and Ca^{2+}-$TFSI^-$ ion pair. (b) Mayer bond orders of C-F, S-N and S-O bonds in $TFSI^-$ and Ca^{2+}-$TFSI^-$ ion pair. The Mayer bond orders of the internal chemical bonds in $TFSI^-$ show an overall decreasing trend after coordinating with Ca^{2+}, indicating reduced stability. Although the average C-F bond order shows a marginal increase, the minimum bond order drops substantially from 1.09 to 0.88, reflecting weaken C-F bonds that are susceptible to scission.

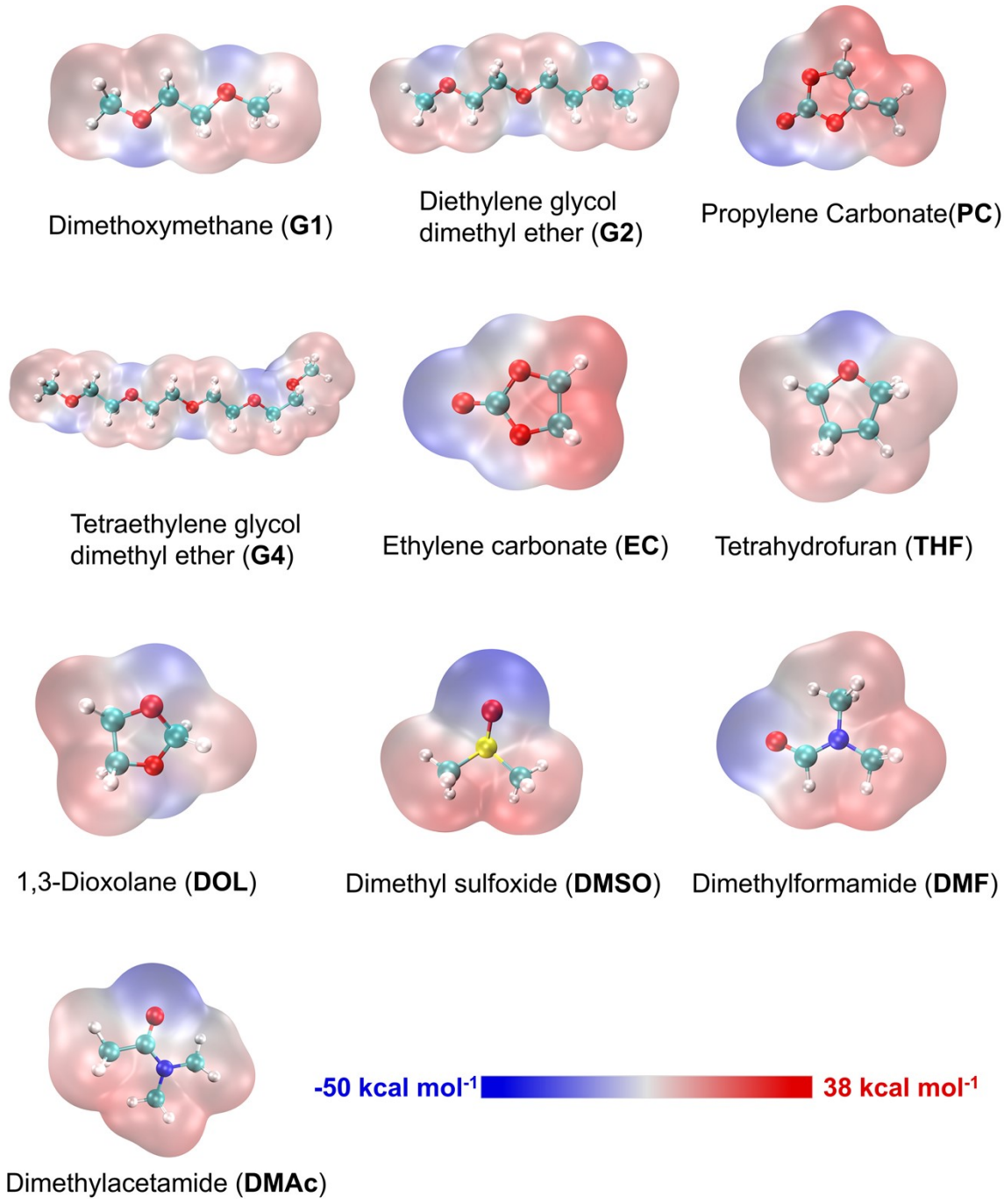

Figure S3. Electrostatic potential (ESP) distribution of various solvent molecules, including G1, G2, G4, PC, EC, THF, DOL, DMSO, DMF, and DMAc.

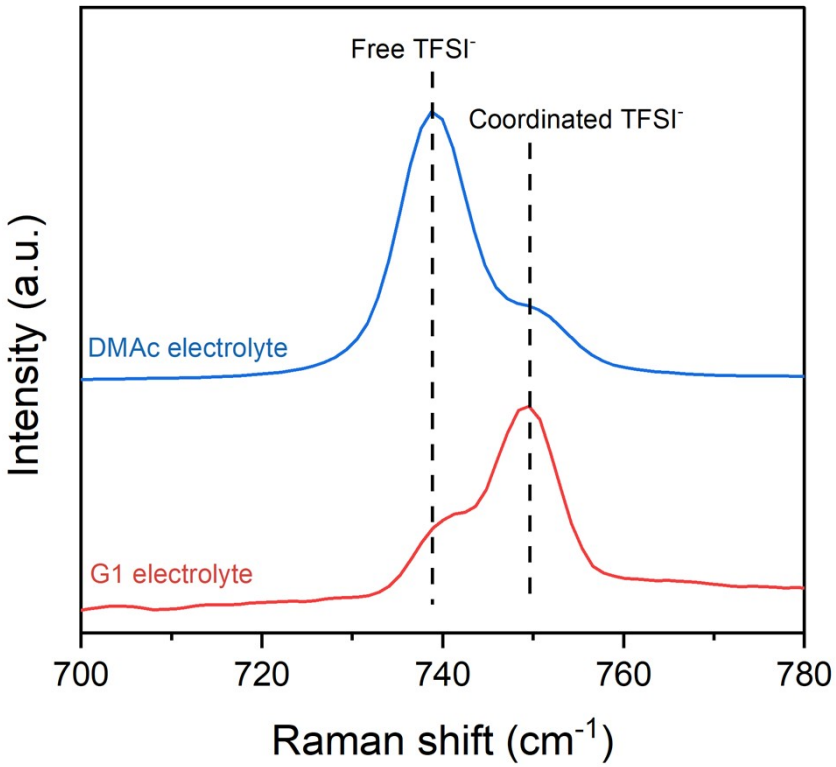

Figure S4. Raman spectra of the S-N-S bending vibration for $TFSI^-$ anions in DMAc electrolyte and G1 electrolyte. Raman peak can be deconvoluted into free and coordinated $TFSI^-$ species.

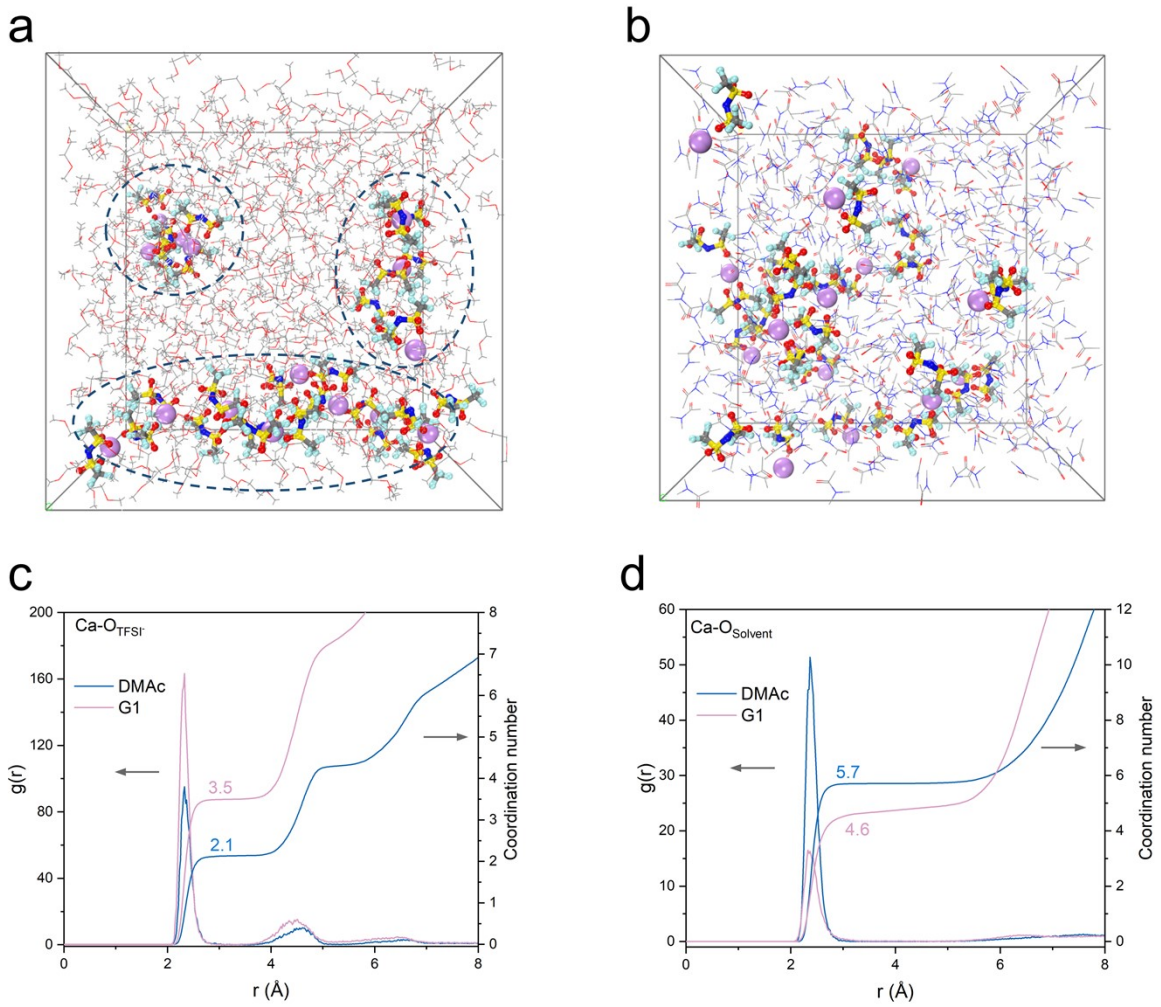

Figure S5. Snapshots from MD simulation boxes of (a) 0.3 M $Ca(TFSI)_2$ G1 and (b) 0.3 M $Ca(TFSI)_2$ DMAc electrolytes. The weakly solvating G1 leads to the aggregation of Ca-$TFSI^-$ ion pairs after reaching thermal equilibration. RDFs and coordination number for (c) Ca-O_{TFSI^-} and (d) Ca-$O_{Solvent}$ in the G1 and DMAc electrolytes, respectively.

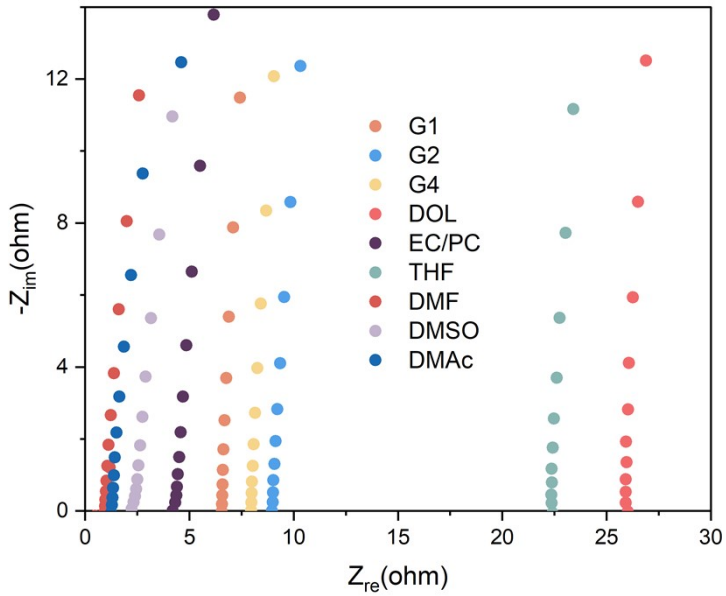

Figure S6. EIS measurements of ionic conductivities for different $Ca(TFSI)_2$-based electrolytes using stainless steel (SS)//SS symmetric cells. Ionic conductivities were calculated according to the following equation:

$$\sigma = \frac{l}{R_s S}$$

where σ (mS cm^{-1}) is the ionic conductivity of the electrolyte, l (cm) represents the distance between electrodes, R_s (ohm) is the solution resistance acquired from the EIS curves. S (cm^{-2}) represents the area of the electrode.

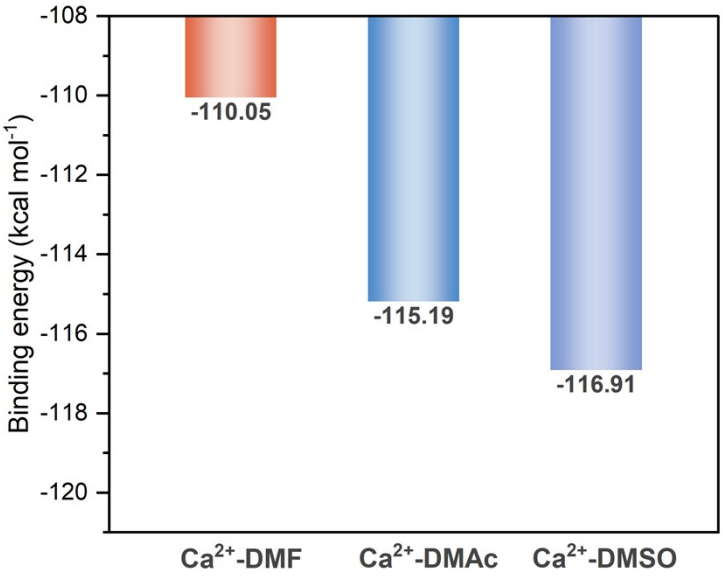

Figure S7. The binding energies of Ca^{2+} with DMF, DMAc and DMSO. The trend in binding energies agrees with the DN-$|ESP_{min}|$ plot, where solvents with stronger solvation abilities locate at the upper right corner in Figure 2b.

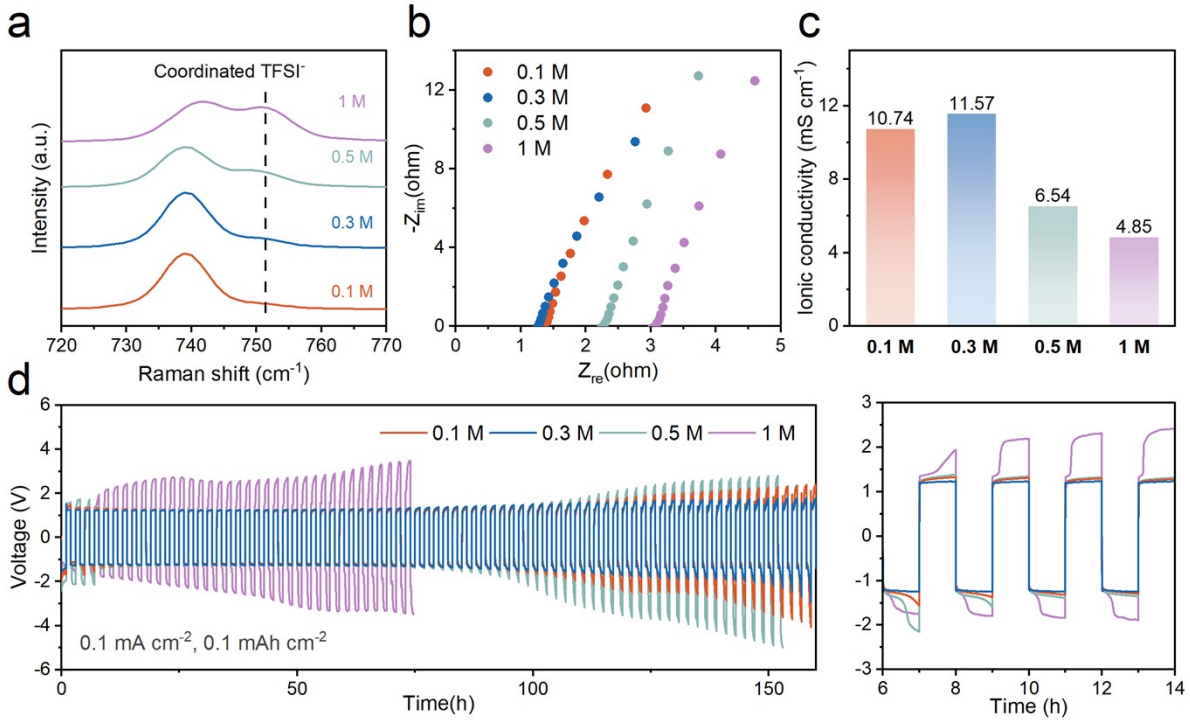

Figure S8. (a) Raman spectra of the S-N-S bending vibration for $TFSI^-$ anions, (b) EIS profiles of SS//SS symmetric cells, (c) calculated ionic conductivities of 0.1, 0.3, 0.5 and 1 M $Ca(TFSI)_2$-DMAc electrolytes, and (d) cycling performance of Ca//Ca symmetric cells in these electrolytes. 0.3 M $Ca(TFSI)_2$-DMAc electrolyte exhibits the largest ionic conductivity, the lowest overpotential for Ca//Ca cycling, and the moderate Ca^{2+}-$TFSI^-$ coordination, which is therefore selected as the baseline electrolyte for subsequent investigations.

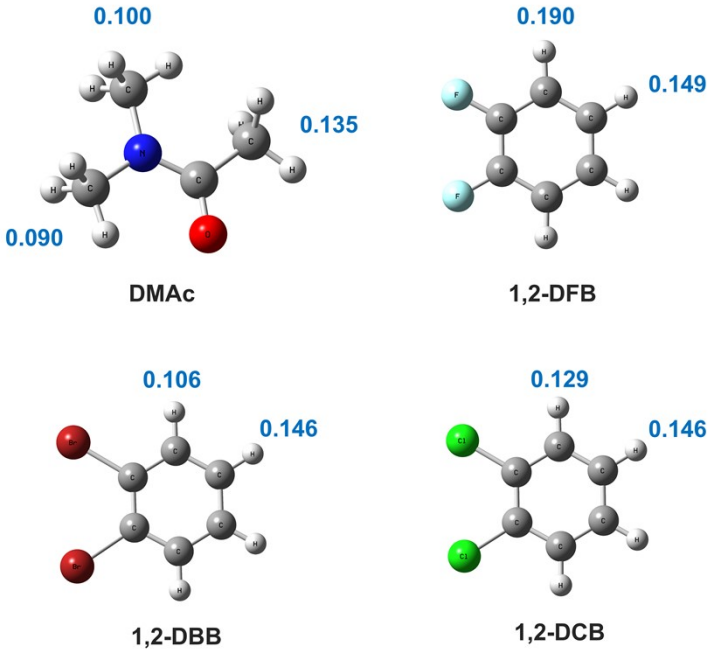

Figure S9. Restrained electrostatic potential (RESP) charges of the hydrogen atoms in DMAc, 1,2-difluorobenzene (1,2-DFB), 1,2-dibromobenzene (1,2-DBB), and 1,2-dichlorobenzene (1,2-DCB) molecules. Equivalent hydrogen atoms with the same charge are labeled only once.

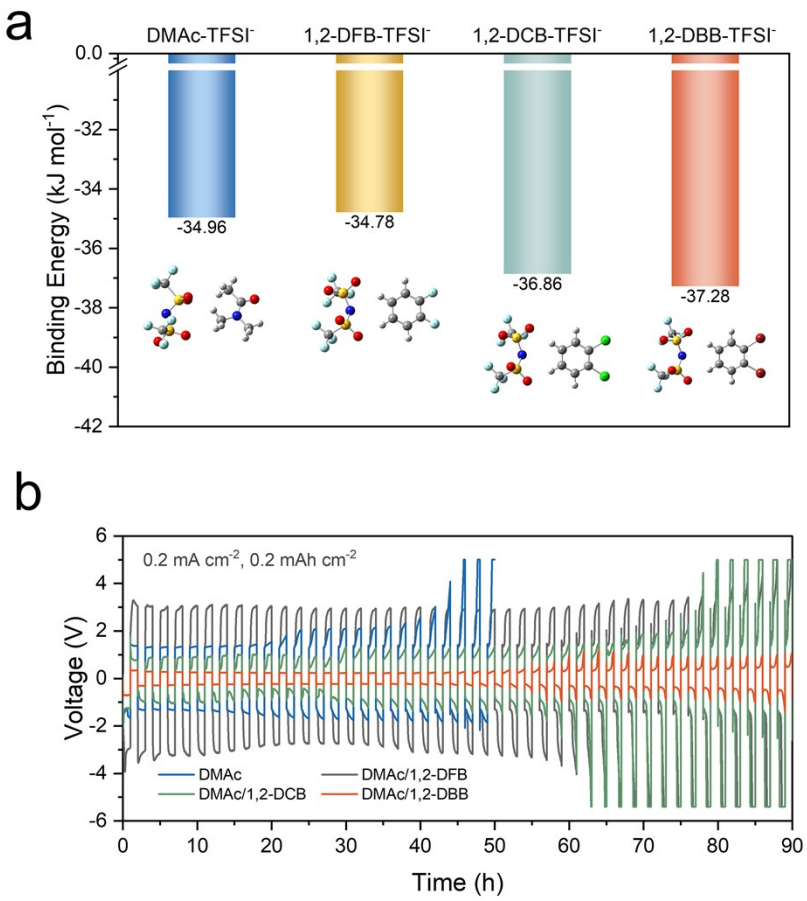

Figure S10. (a) Binding energies of different solvent or additives (*i.e.,* DMAc, 1,2-DFB, 1,2-DCB, 1,2-DBB) with $TFSI^-$ anions (Inset: optimized geometries of the binding complexes). (b) Cycling performance of Ca//Ca symmetric cells at 0.2 mA cm^{-2}/0.2 mAh cm^{-2} in $Ca(TFSI)_2$ DMAc electrolytes with 0.5 vol% halogenated benzene additives. DMAc/1,2-DBB presents the optimal performance.

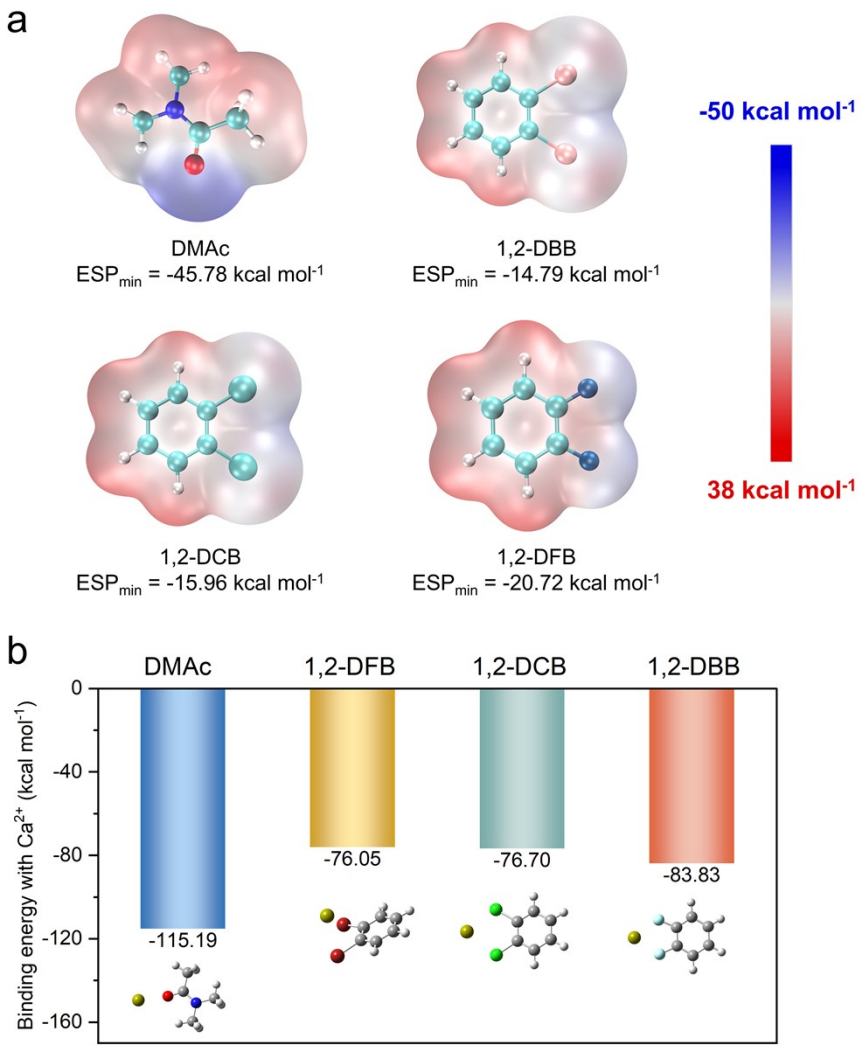

Figure S11. (a) ESP distribution and ESP$_{min}$ of DMAc, 1,2-DBB, 1,2-DCB and 1,2-DFB. (b) Binding energies of Ca^{2+} with DMAc, 1,2-DBB, 1,2-DCB and 1,2-DFB (Inset: optimized geometries of binding complexes).

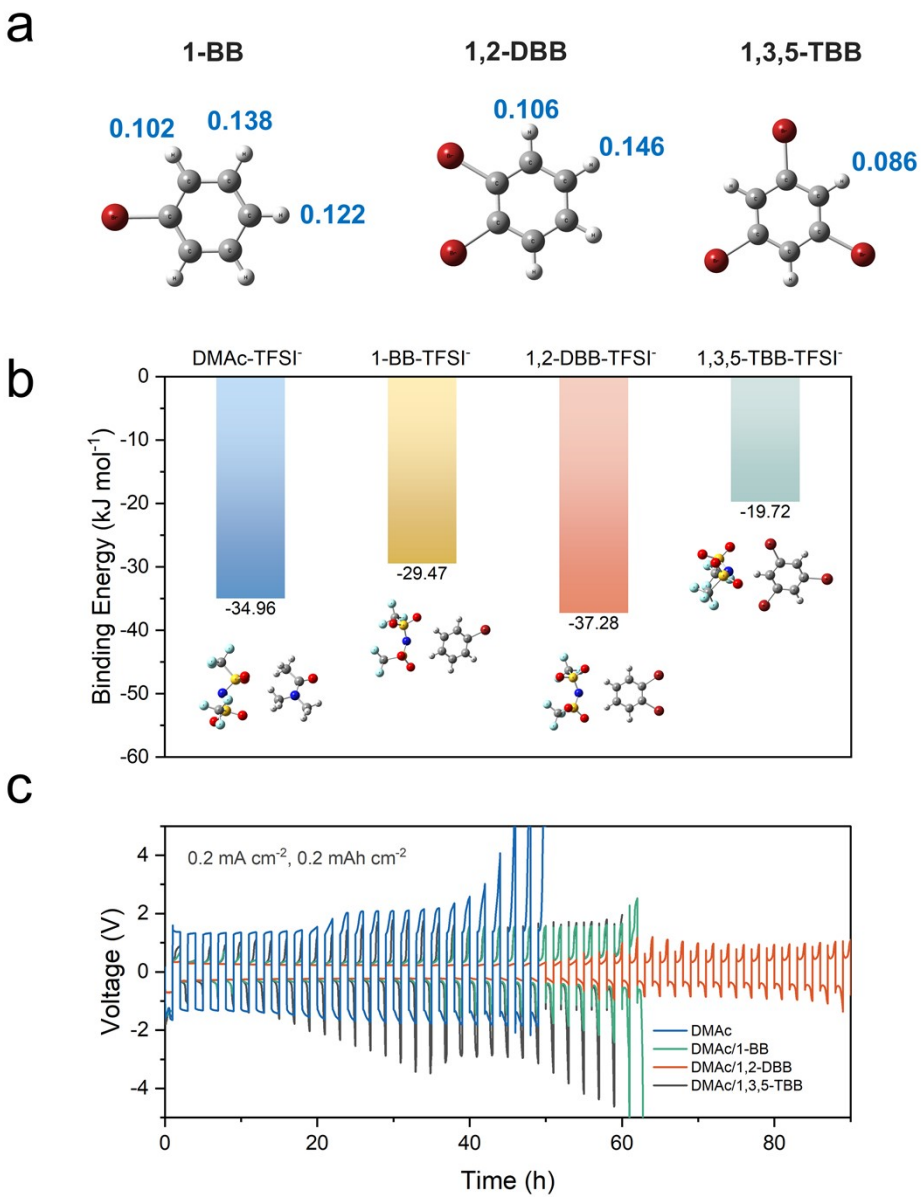

Figure S12. (a) RESP charges of hydrogen atoms in 1-Bromobenzene (1-BB), 1,2-DBB and 1,3,5-Tribromobenzene (1,3,5-TBB). Equivalent hydrogen atoms with the same charge are labeled only once. (b) Binding energies between different electrolyte components with the $TFSI^-$ anion (Inset: optimized geometries of binding complexes). (c) Cycling performance of Ca//Ca symmetric cells at 0.2 mA cm^{-2}/0.2 mAh cm^{-2} with various bromobenzene additives at a fixed addition of 0.5 vol% (0.5 wt% for 1,3,5-TBB). The number of bromine substituents and molecular symmetry influence the partial charges on hydrogen atoms, resulting in lower binding energies with $TFSI^-$ for 1-BB and 1,3,5-TBB. Ca//Ca symmetric cells in these two additives display inferior cycling performance to that of DMAc baseline electrolyte.

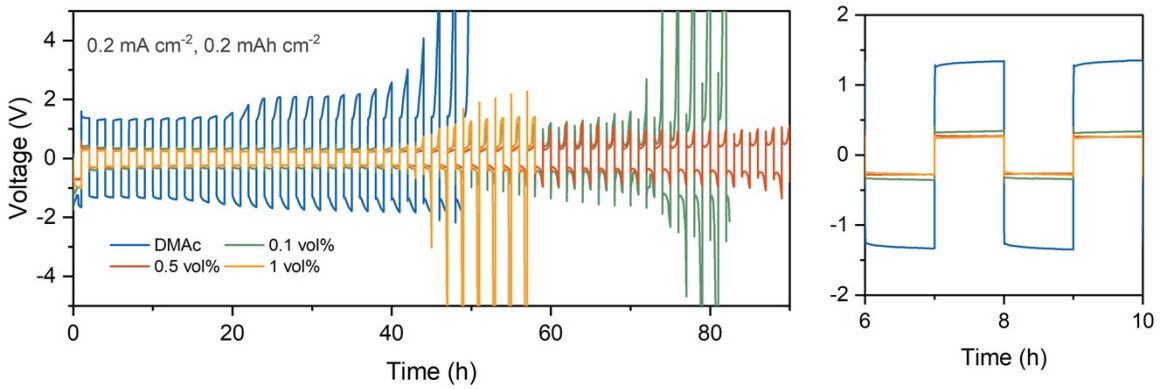

Figure S13. Cycling performance of Ca//Ca symmetric cells at 0.2 mA cm^{-2}/0.2 mAh cm^{-2} with different volume ratios of 1,2-DBB. Although the overpotential steadily decreases with higher concentration of 1,2-DBB, cycling stability concurrently diminishes. A 0.5 vol% 1,2-DBB addition was selected as the optimal formula.

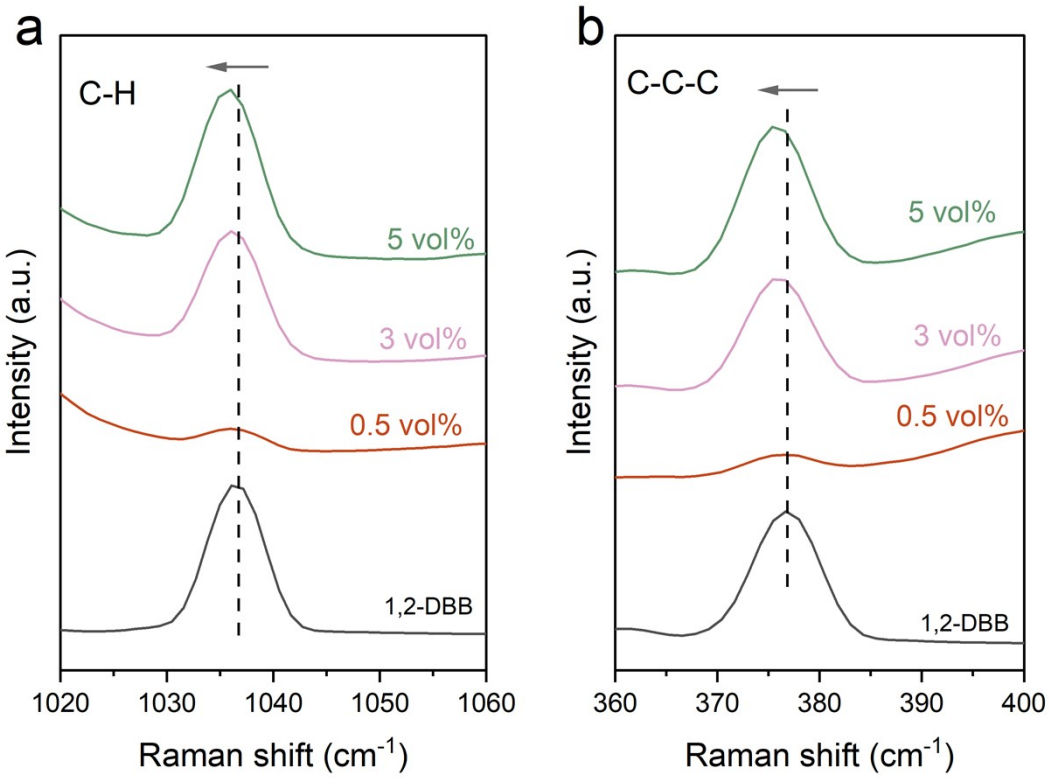

Figure S14. Raman spectra of (a) C-H in-plane bending and (b) C-C-C out-of-plane bending vibrations of pure 1,2-DBB and 0.5M $Ca(TFSI)_2$ DMAc electrolytes with different 1,2-DBB concentrations (*i.e.,* 0.5 vol.%, 3 vol.%, 5 vol.%).

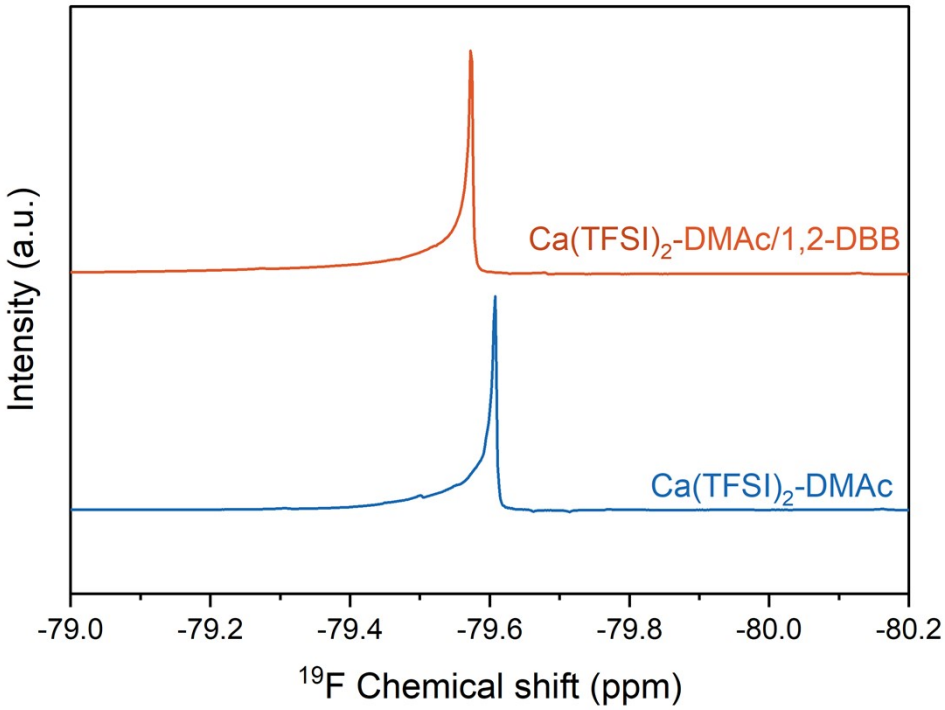

Figure S15. ^{19}F NMR spectra of DMAc and DMAc/1,2-DBB electrolytes.

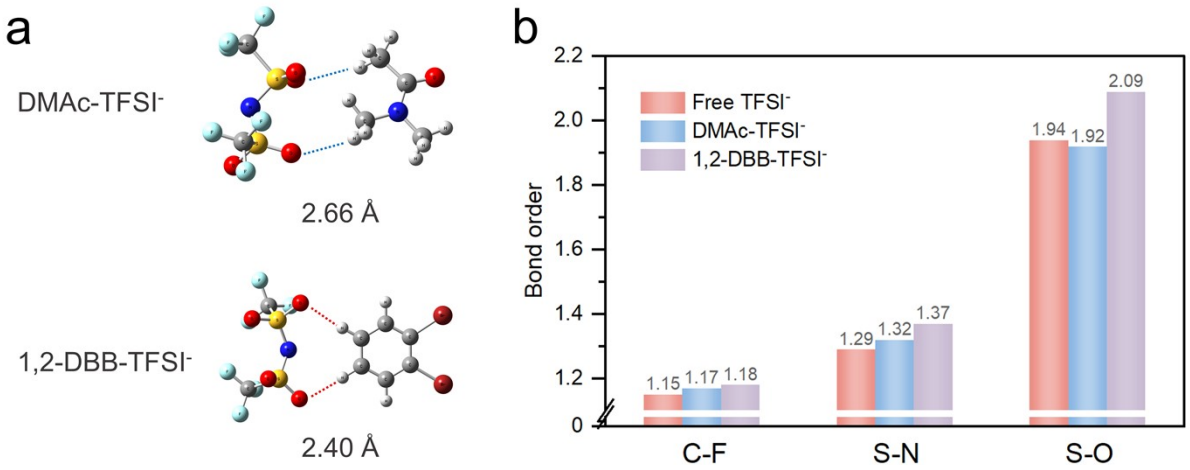

Figure S16. (a) Optimized binding configurations and C–H···O hydrogen bond lengths for DMAc-TFSI$^-$ and 1,2-DBB-TFSI$^-$ complexes. (b) Mayer bond orders of C-F, S-N and S-O bonds in TFSI$^-$ under different states.

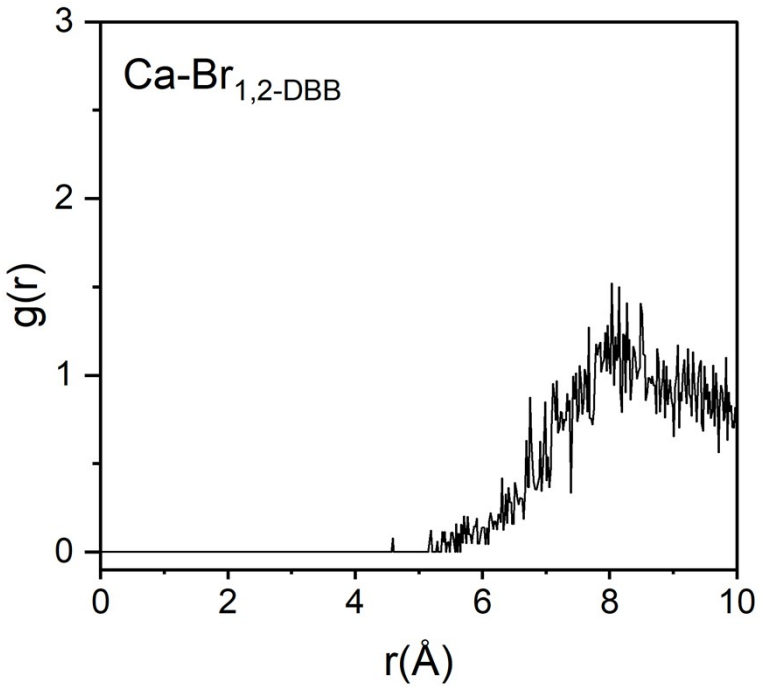

Figure S17. The RDF plot for Ca-Br (1,2-DBB) in the DMAc/1,2-DBB electrolyte.

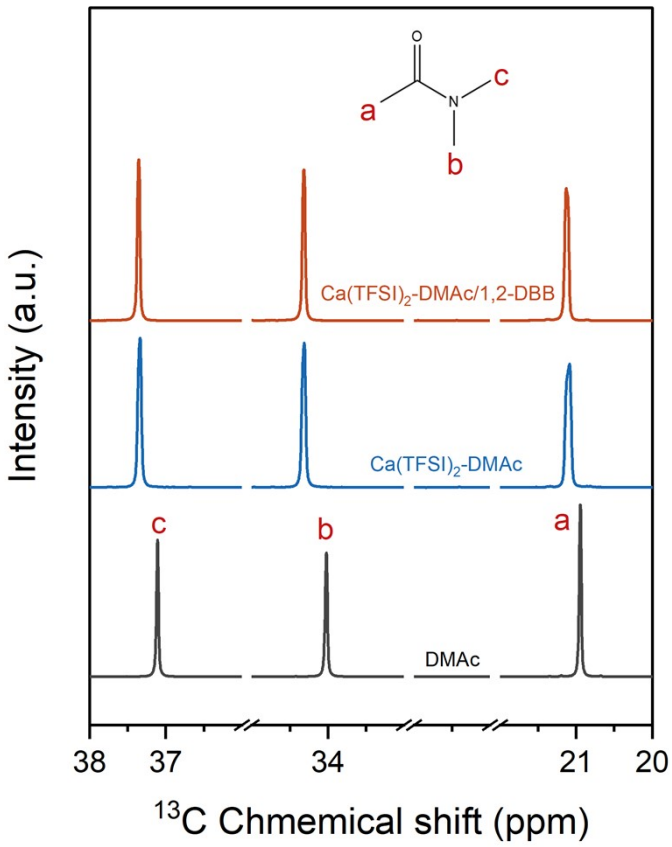

Figure S18. ^{13}C NMR spectra of pure DMAc, $Ca(TFSI)_2$ DMAc electrolyte, and $Ca(TFSI)_2$ DMAc/1,2-DBB electrolyte. Coordination with Ca^{2+} reduces the electron density around the C atoms in DMAc, leading to a downfield shift of the peak. Upon the addition of 1,2-DBB, a further downfield shift is observed, indicating the enhanced coordination of DMAc.

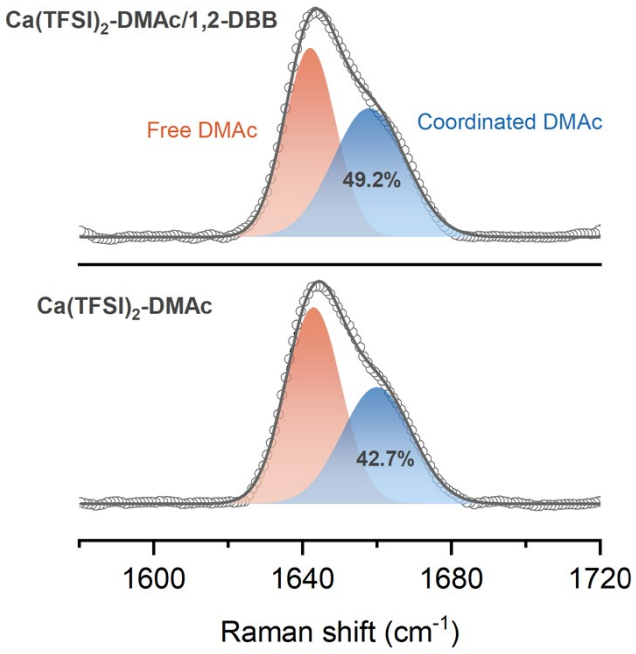

Figure S19. Raman spectra of DMAc and DMAc/1,2-DBB electrolytes. The Raman peaks are deconvoluted into free DMAc and coordinated DMAc.

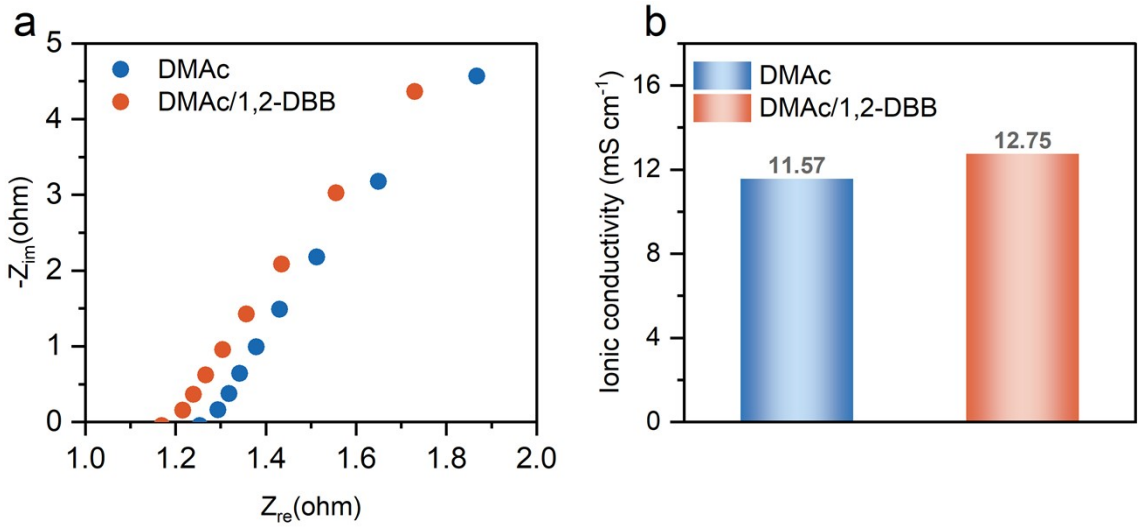

Figure S20. (a) EIS plots of stainless steel (SS)//SS symmetric cells in DMAc and DMAc1,2-DBB electrolytes, (b) the calculated ionic conductivities.

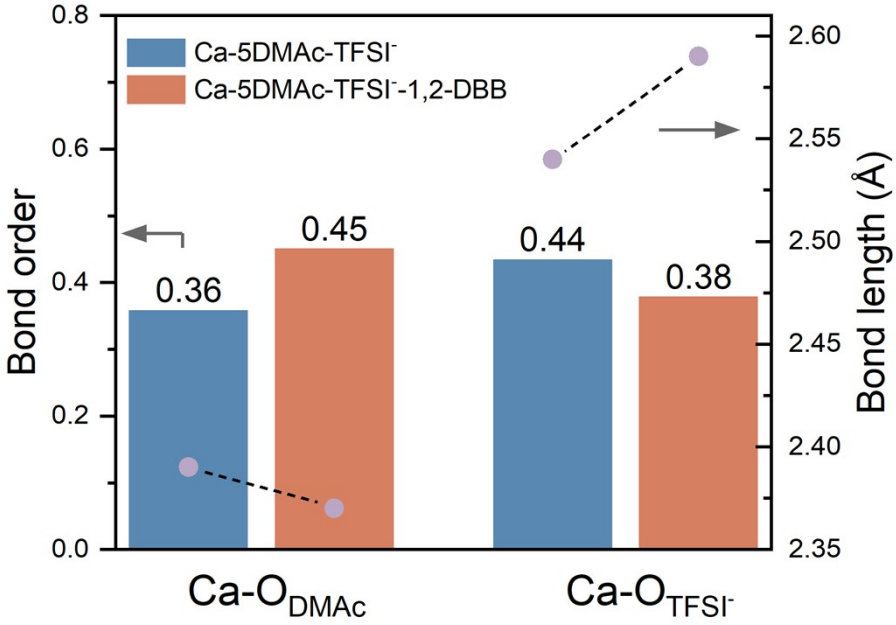

Figure S21. Bond order and length of Ca-O (Ca-DMAc-TFSI$^-$) in the solvation structures with (red) and without (blue) 1,2-DBB.

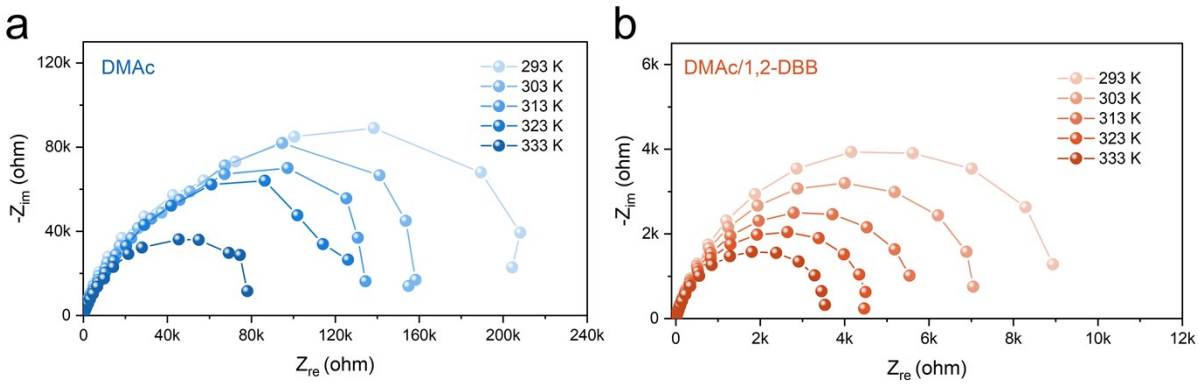

Figure S22. EIS of Ca//Ca symmetric cells at different temperatures in (a) DMAc and (b) DMAc/1,2-DBB electrolytes. The charge transfer resistance (R_{CT}) primarily reflects the desolvation energy barriers, thus the desolvation energy was calculated from the Arrhenius equation:

$$\frac{1}{R_{CT}} = A\exp\left(\frac{-E_a}{RT}\right)$$

Where E_a, R_{CT}, A, R, and T represent the desolvation energy, charge transfer resistance, the frequency factor, the gas constant, and the absolute temperature, respectively.

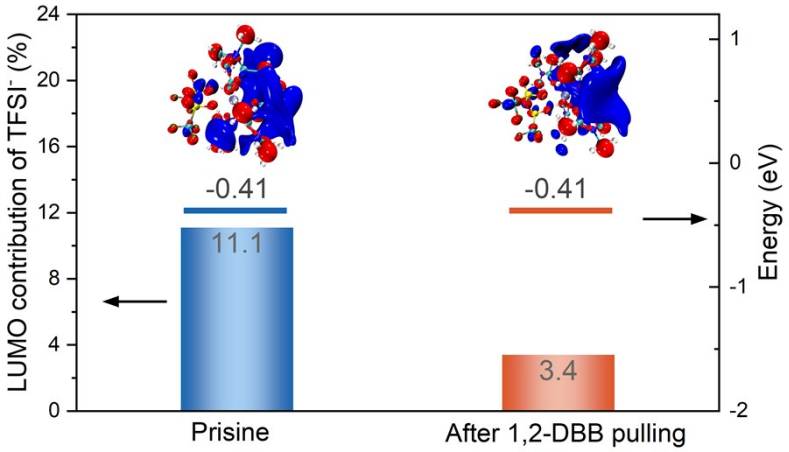

Figure S23. LUMO energies and $TFSI^-$ LUMO contribution ratios of Ca-5DMAc-$TFSI^-$ solvation shell before and after the 1,2-DBB pulling effect.

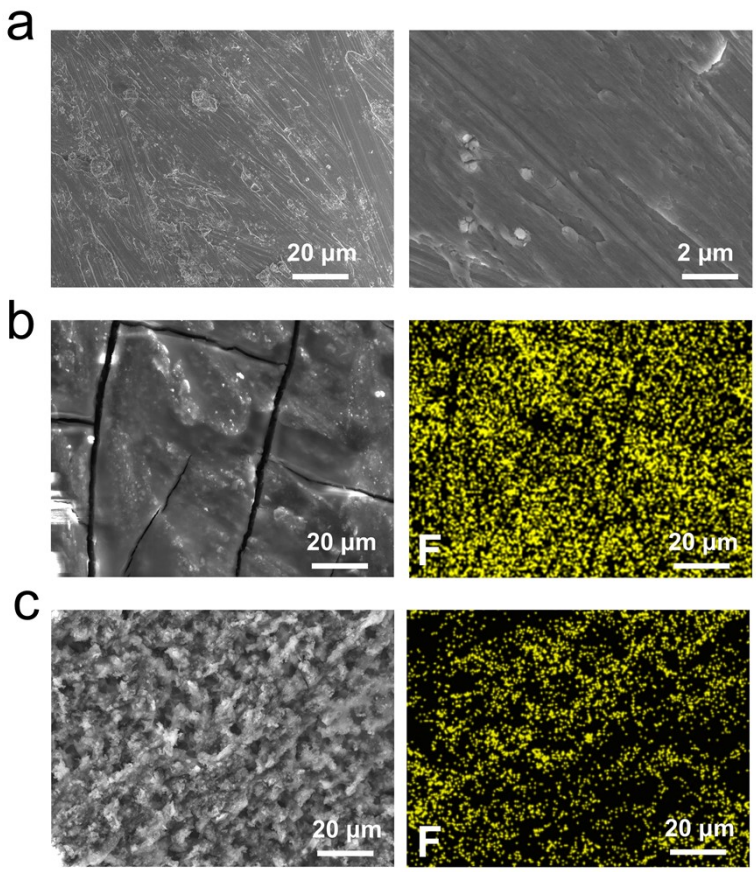

Figure S24. SEM images and corresponding EDS mappings of the (a) pristine Ca foil and Ca metal anodes after 20 cycles in (b) DMAc and (c) DMAc/1,2-DBB electrolytes.

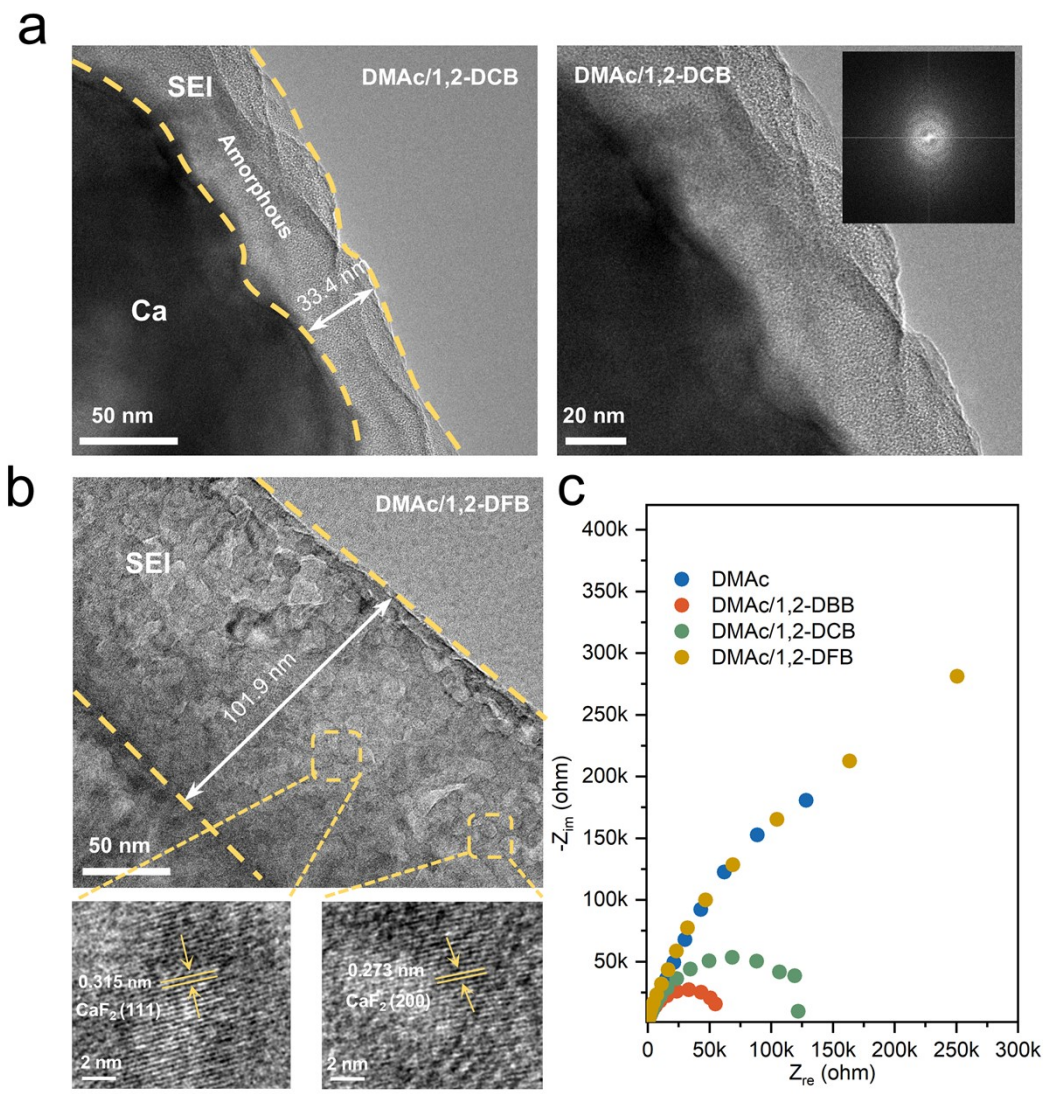

Figure S25. HRTEM images of SEI layers formed in the (a) DMAc/1,2-DCB and (b) DMAc/1,2-DFB electrolytes. (c) Nyquist plots of Ca//Ca symmetric cells after 20 cycles in DMAc, DMAc/1,2-DBB, DMAc/1,2-DCB and DMAc/1,2-DFB electrolytes at 0.1 mA cm^{-2} and 0.1 mAh cm^{-2}. 1,2-DCB exhibits stronger binding affinities with $TFSI^-$ than DMAc (**Figure S10**), resulting in the amorphous, organic-rich SEI. In contrast, 1,2-DFB exhibits the weakest anion-decoupling ability, coupled with its intrinsic fluorine-rich nature, leading to a substantially thicker SEI (~101.9 nm) dominated by highly insulating CaF_2 nanocrystals. Moreover, the trend in EIS interfacial resistance is consistent with SEI properties.

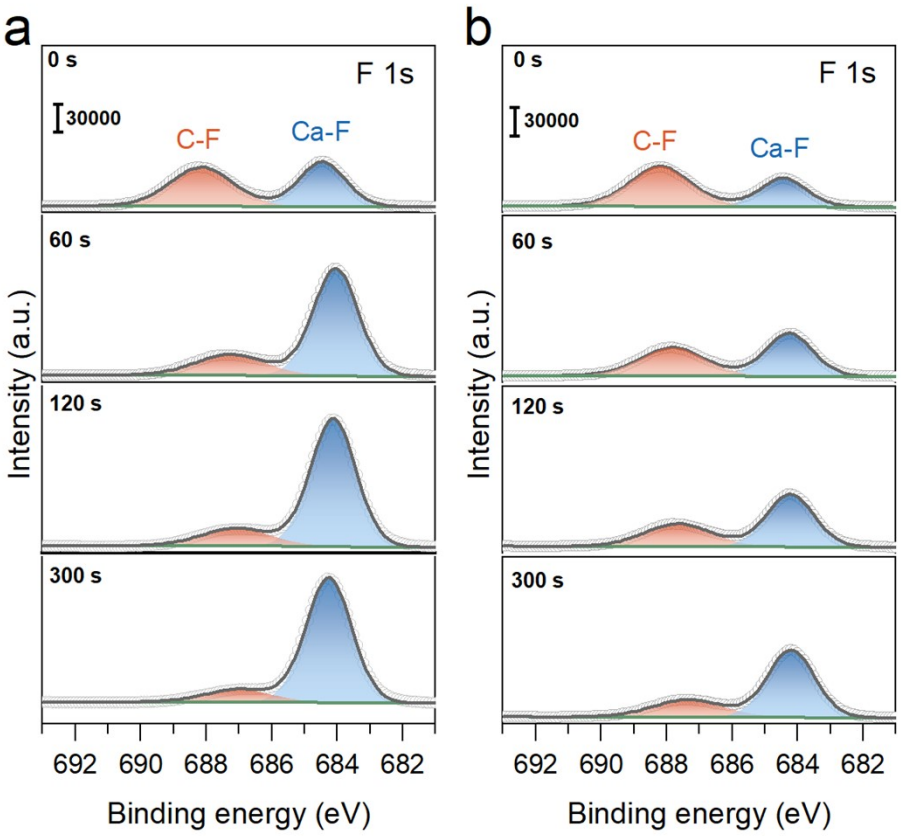

Figure S26. F 1s XPS depth profiles of cycled Ca anodes in (a) DMAc and (b) DMAc/1,2-DBB electrolytes.

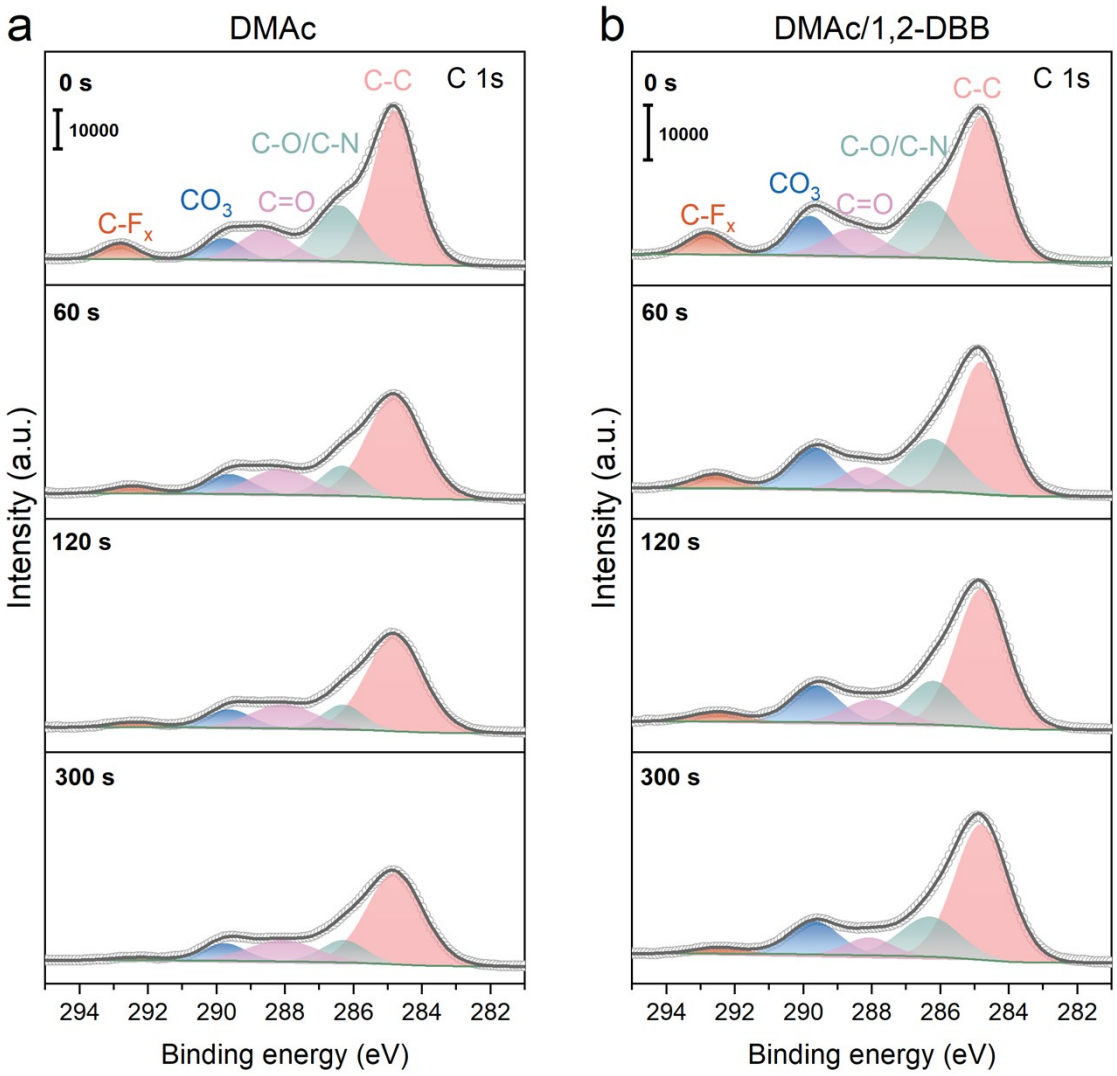

Figure S27. C 1s XPS depth profiles of cycled Ca anodes in (a) DMAc and (b) DMAc/1,2-DBB electrolytes.

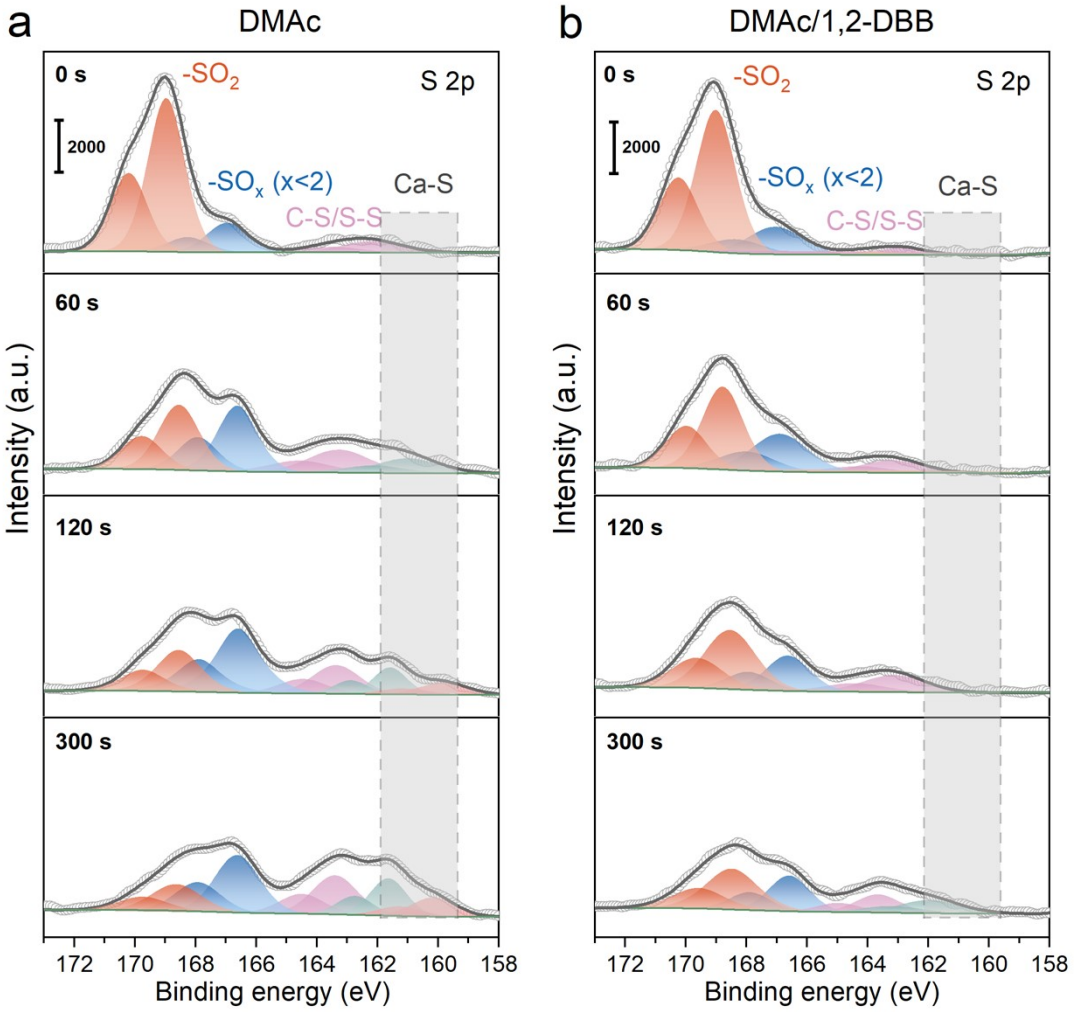

Figure S28. XPS depth profiles of S 2p for Ca anodes after 20 cycles in Ca//Ca symmetric cells with (a) DMAc and (b) DMAc/1,2-DBB electrolytes. The significant Ca-S signals from $TFSI^-$ decomposition are observed in the DMAc electrolyte, whereas in the DMAc/1,2-DBB electrolyte, these signals are virtually absent.

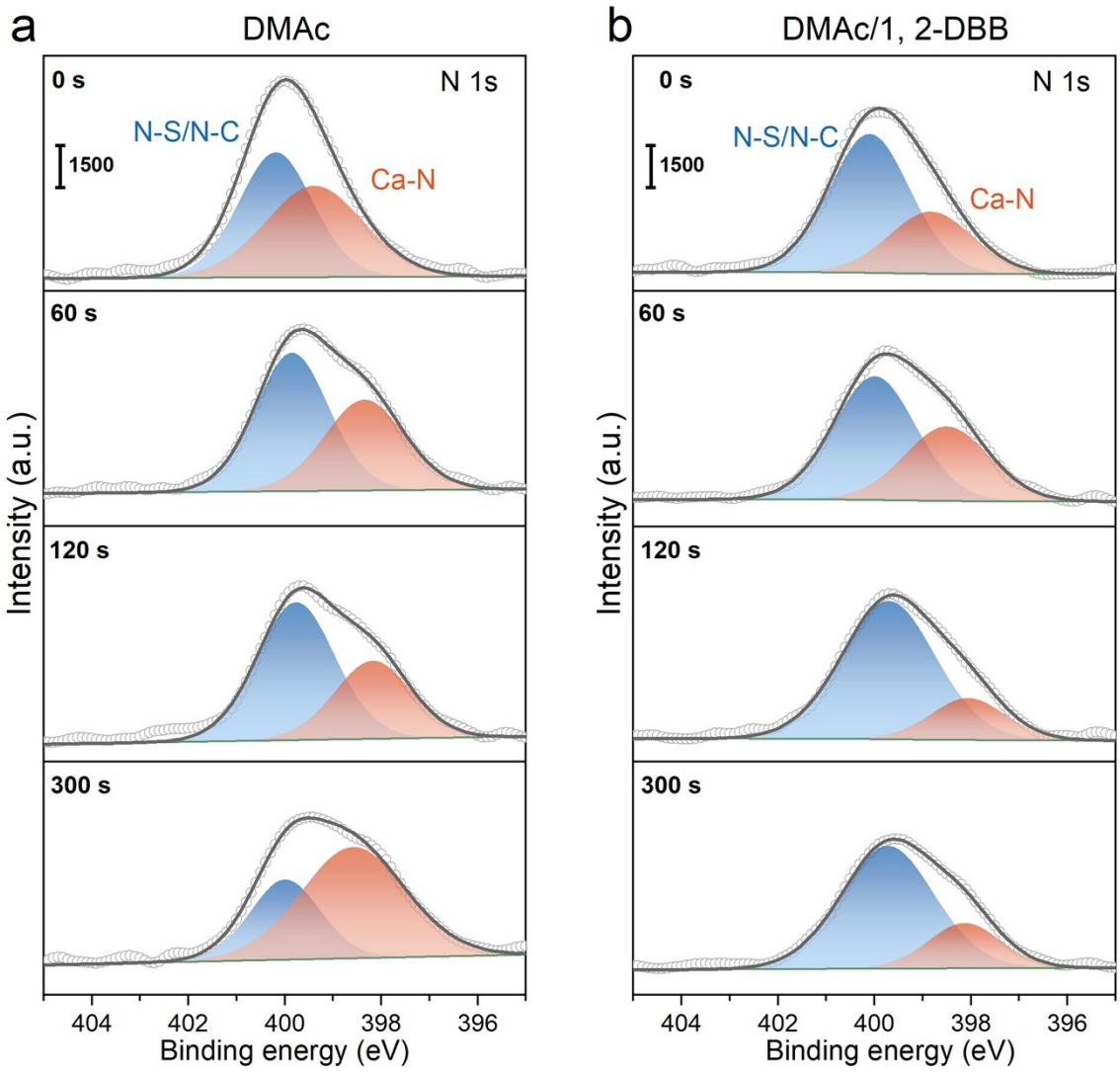

Figure S29. XPS depth profiles of N 1s for Ca anodes after 20 cycles in Ca//Ca symmetric cells with (a) DMAc and (b) DMAc/1,2-DBB electrolytes. The enhanced S-N and significantly weakened Ca-N signals in the DMAc/1,2-DBB electrolyte are consistent with the increased stability of the S-N bond in $TFSI^-$.

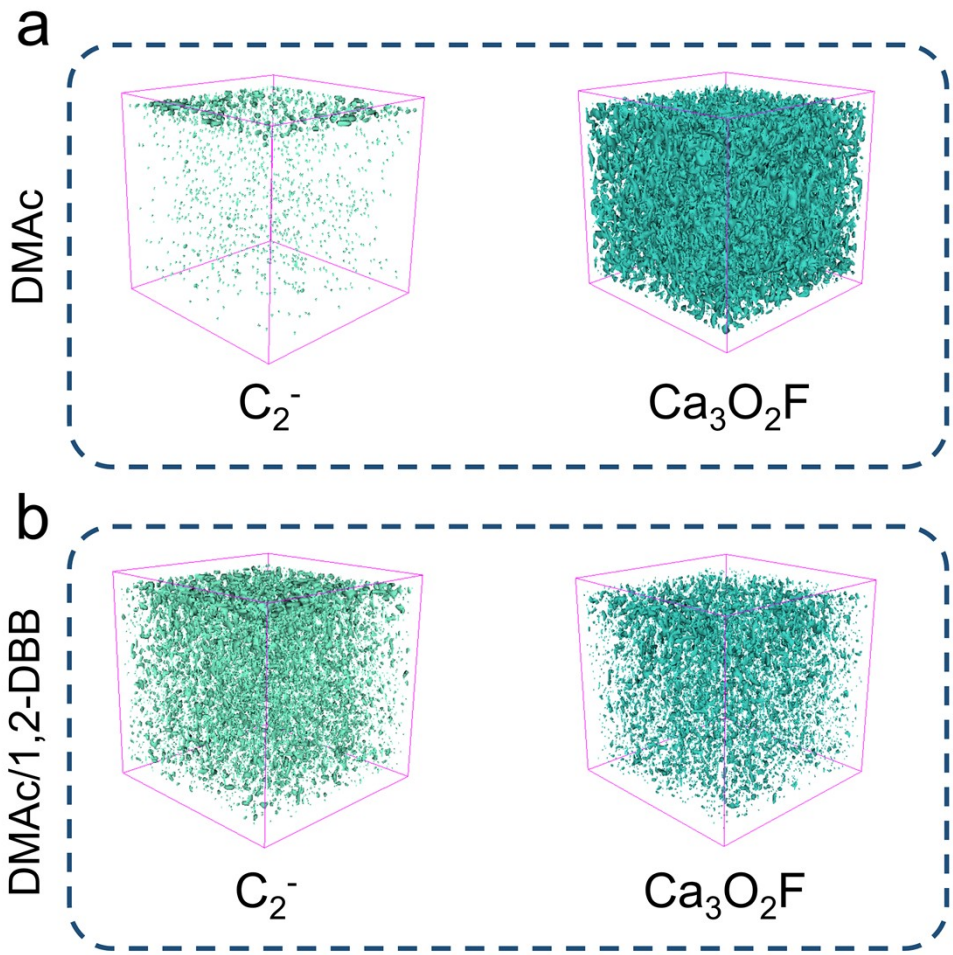

Figure S30. TOF-SIMS 3D reconstruction of C_2^- (organic compounds) and Ca_3O_2F (inorganic compound) distributions in SEI layers formed in (a) DMAc and (b) DMAc/1,2-DBB electrolytes.

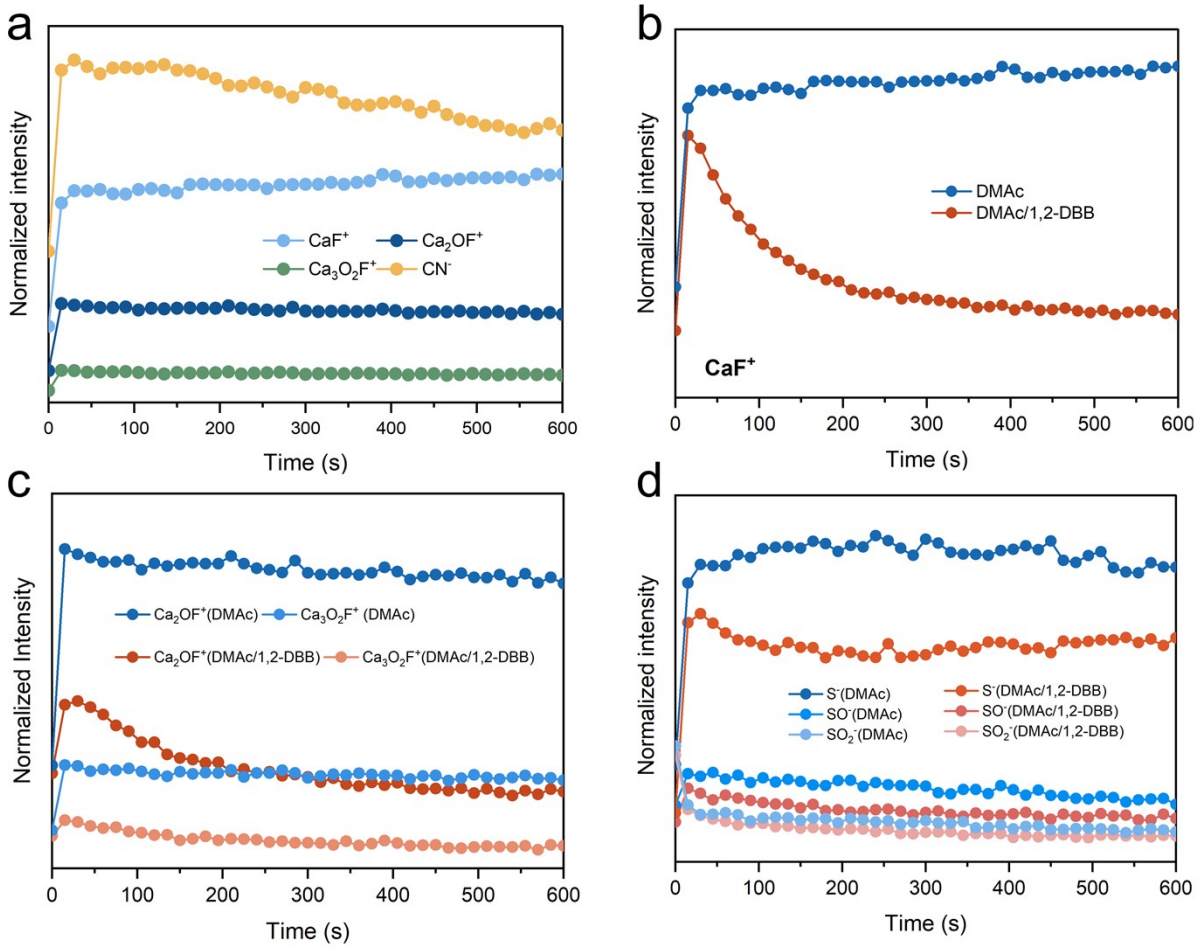

Figure S31. (a) TOF-SIMS depth profiles of SEI species formed in the DMAc electrolyte. Comparisons of (b) CaF^+, (c) Ca_2OF^+, $Ca_3O_2F^+$ and (d) sulfur-containing species (S^-, SO^-, SO_2^-) in the SEIs formed in DMAc (blue) and DMAc/1,2-DBB (red) electrolytes.

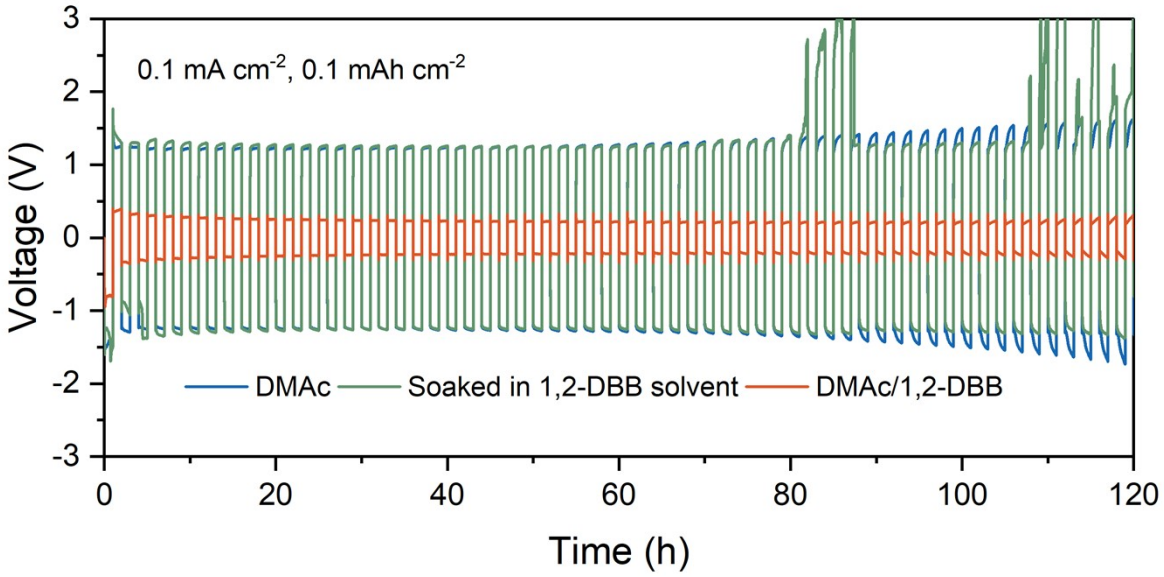

Figure S32. Cycling performance of Ca//Ca symmetric cells at 0.1 mA cm^{-2}/0.1 mAh cm^{-2}. The voltage profiles for Ca electrodes soaked in 1,2-DBB solvent for 24 hours are almost identical to those for pristine Ca electrodes, indicating that 1,2-DBB does not undergo spontaneous adsorption or chemical reaction on the Ca metal surface.

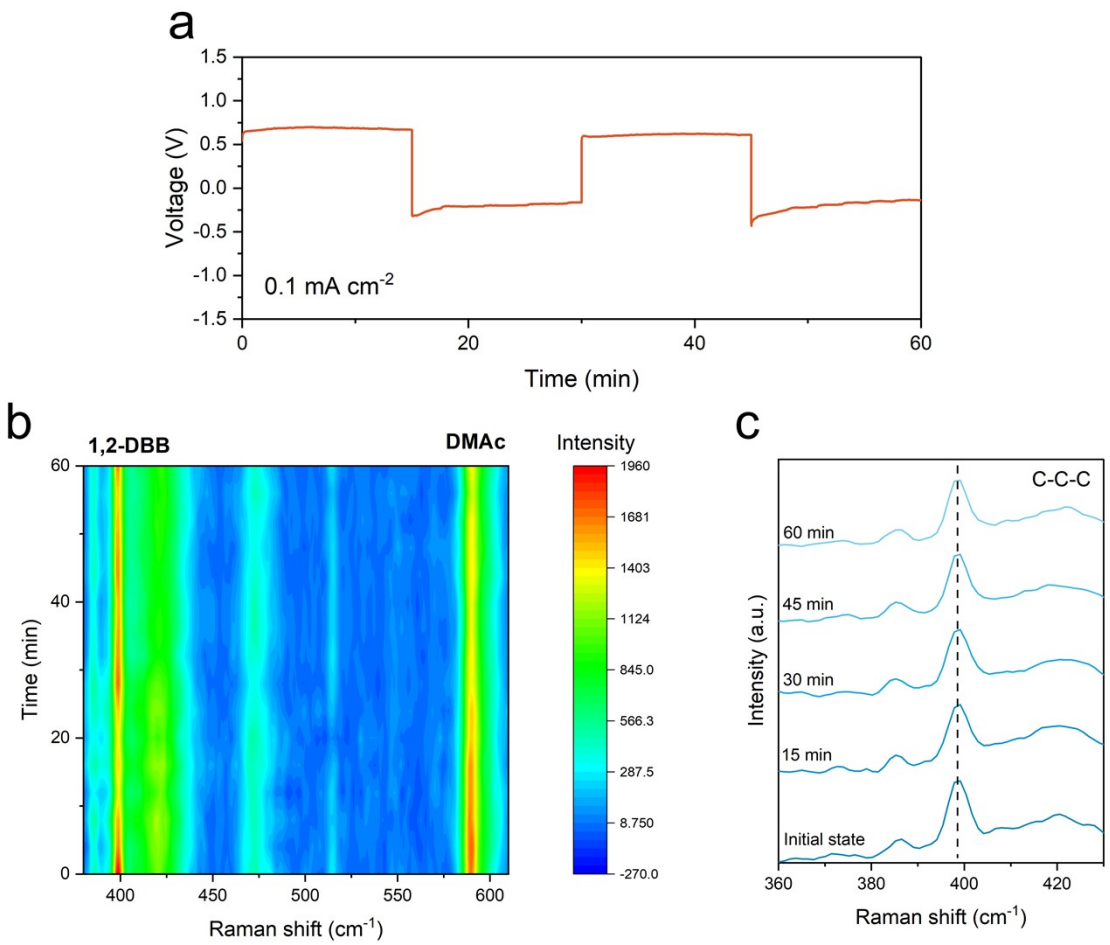

Figure S33. (a) Voltage profiles of Ca//Ca symmetric cells in the DMAc/1,2-DBB electrolyte at 0.1 mA cm^{-2}, (b) the corresponding in-situ Raman spectra of the electrolyte during cycling, (c) no apparent changes in the 1,2-DBB signal during the whole test.

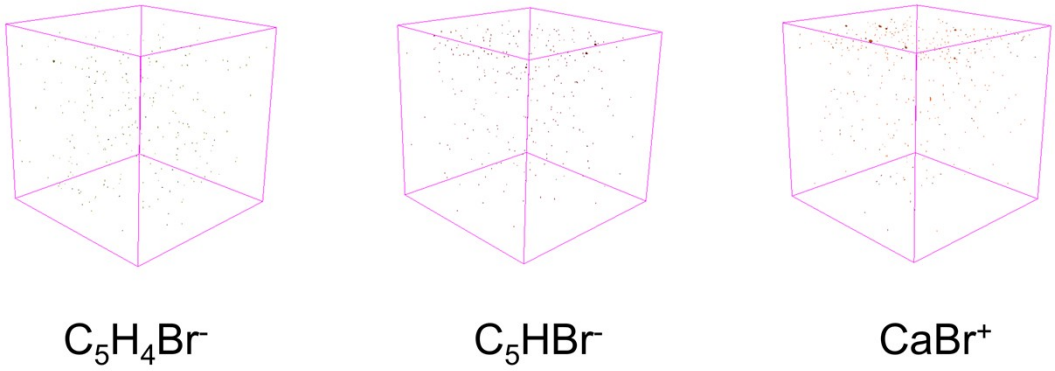

Figure S34. TOF-SIMS 3D reconstruction of $C_5H_4Br^-$, C_5HBr^- and $CaBr^+$ distributions in the SEI that formed in the DMAc/1,2-DBB electrolyte.

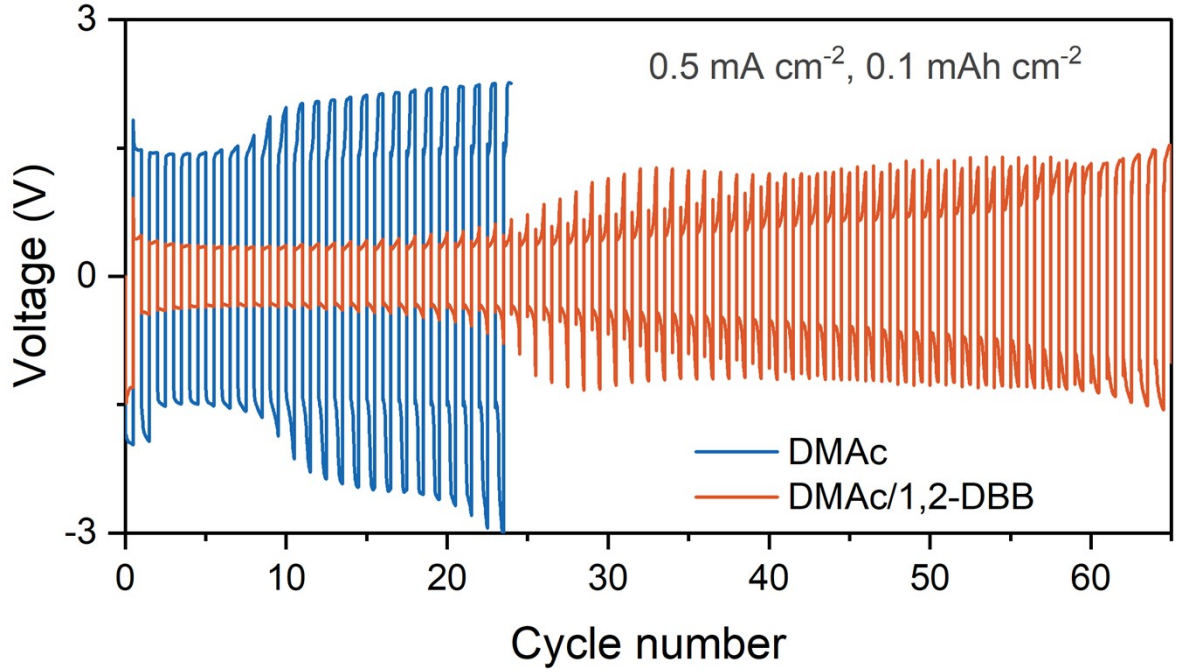

Figure S35. Cycling performance of Ca//Ca symmetric cells at 0.5 mA cm^{-2}/0.1 mAh cm^{-2} in the DMAc (blue) and DMAc/1,2-DBB (red) electrolytes.

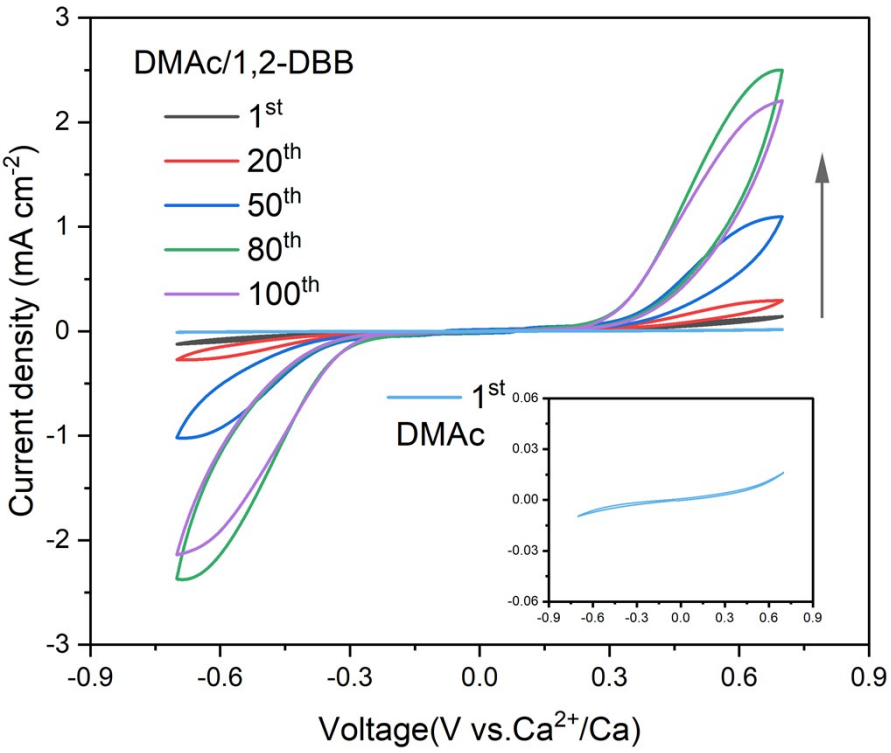

Figure S36. CV curves of Ca//Ca symmetric cells in DMAc/1,2-DBB electrolyte and DMAc electrolyte (inset).

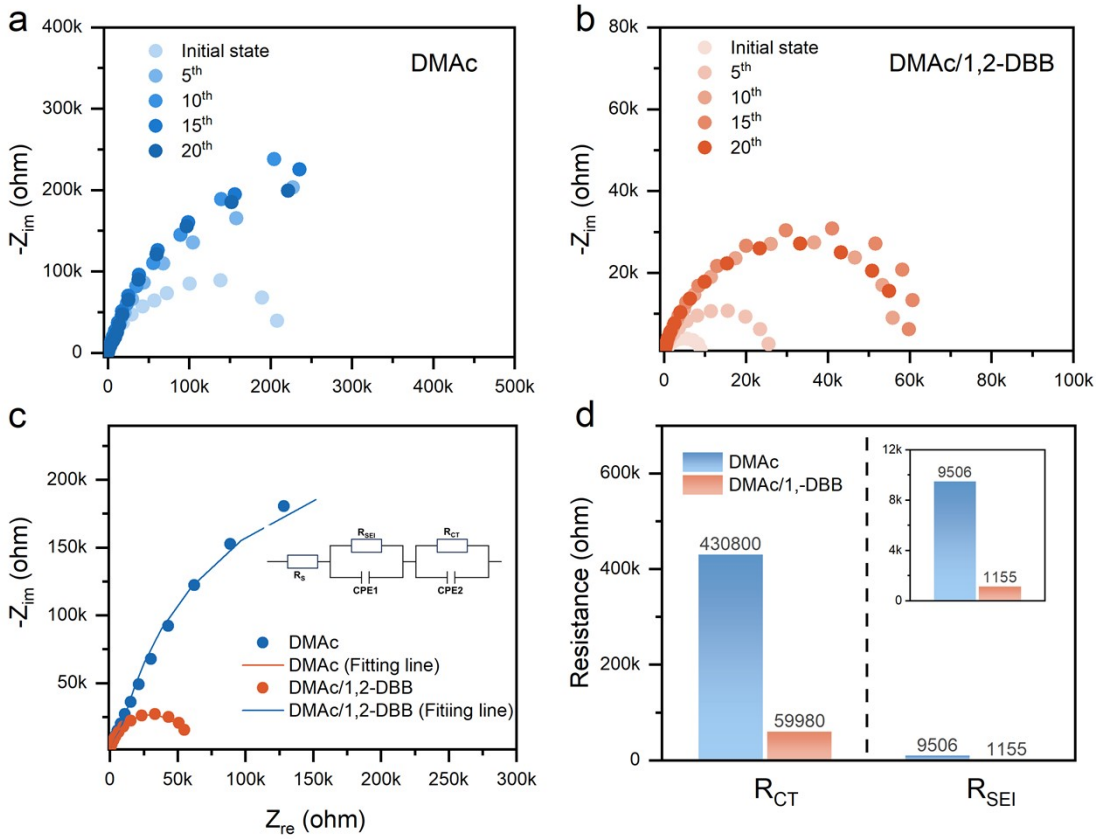

Figure S37. Nyquist plots of Ca//Ca symmetric cells at the initial state and after the 5th, 10th, 15th, and 20th cycles in the (a) DMAc electrolyte and (b) DMAc/1,2-DBB electrolyte. (c) Nyquist plots of Ca//Ca symmetric cells after 20 cycles in above electrolytes. The data were fit (solid line) with the indicated equivalent circuit, where R_S, R_{CT}, R_{SEI} represent the solution resistance, charge transfer resistance and SEI resistance. (d) R_{CT}, R_{SEI} for Ca electrodes after 20 cycles in the above two electrolytes.

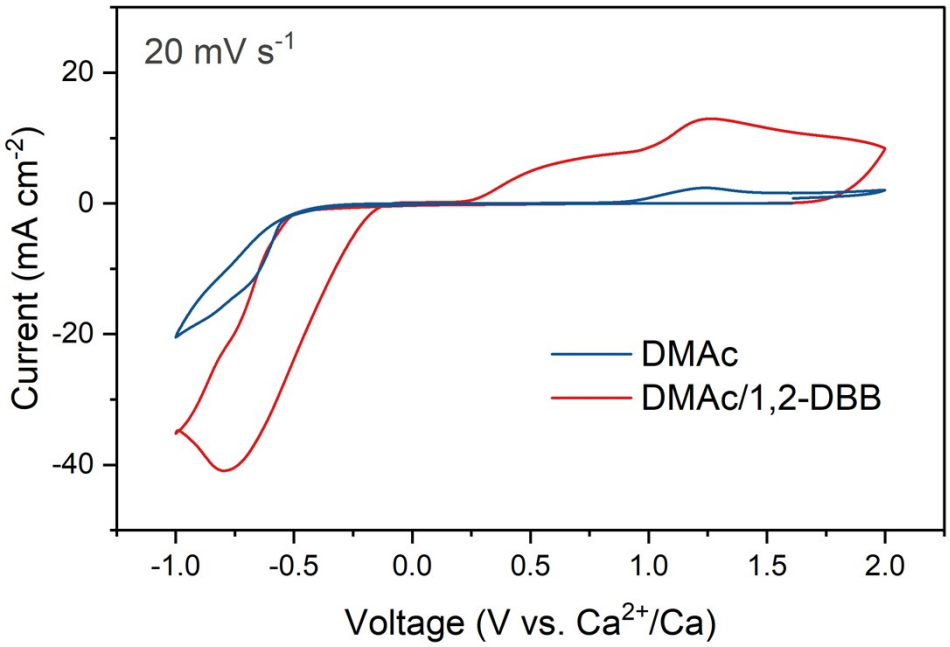

Figure S38. CV curves of Ca//carbon paper (CC) half cells in DMAc and DMAc/1,2-DBB electrolytes at a scan rate of 20 mV s^{-1}.

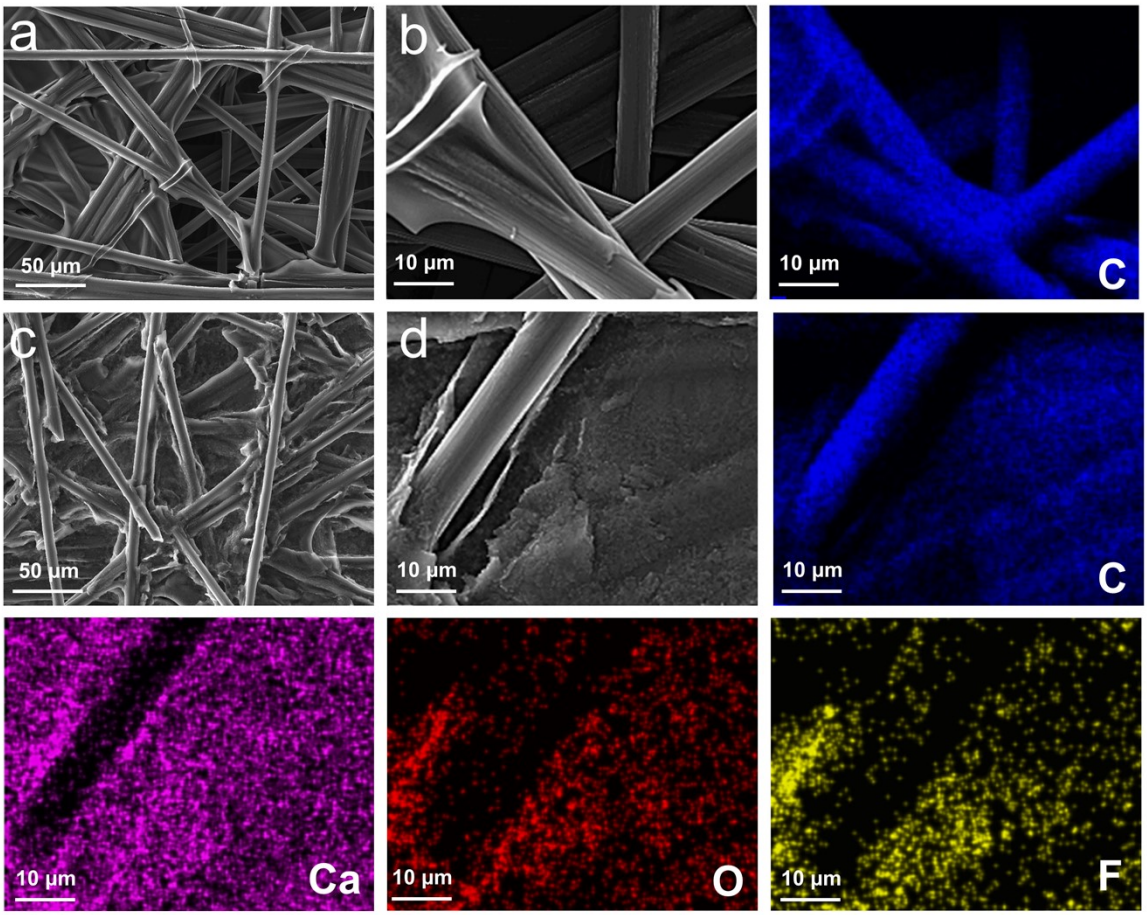

Figure S39. SEM images and corresponding EDS mappings of the (a, b) carbon cloth current collector and (c, d) Ca deposits on carbon cloth.

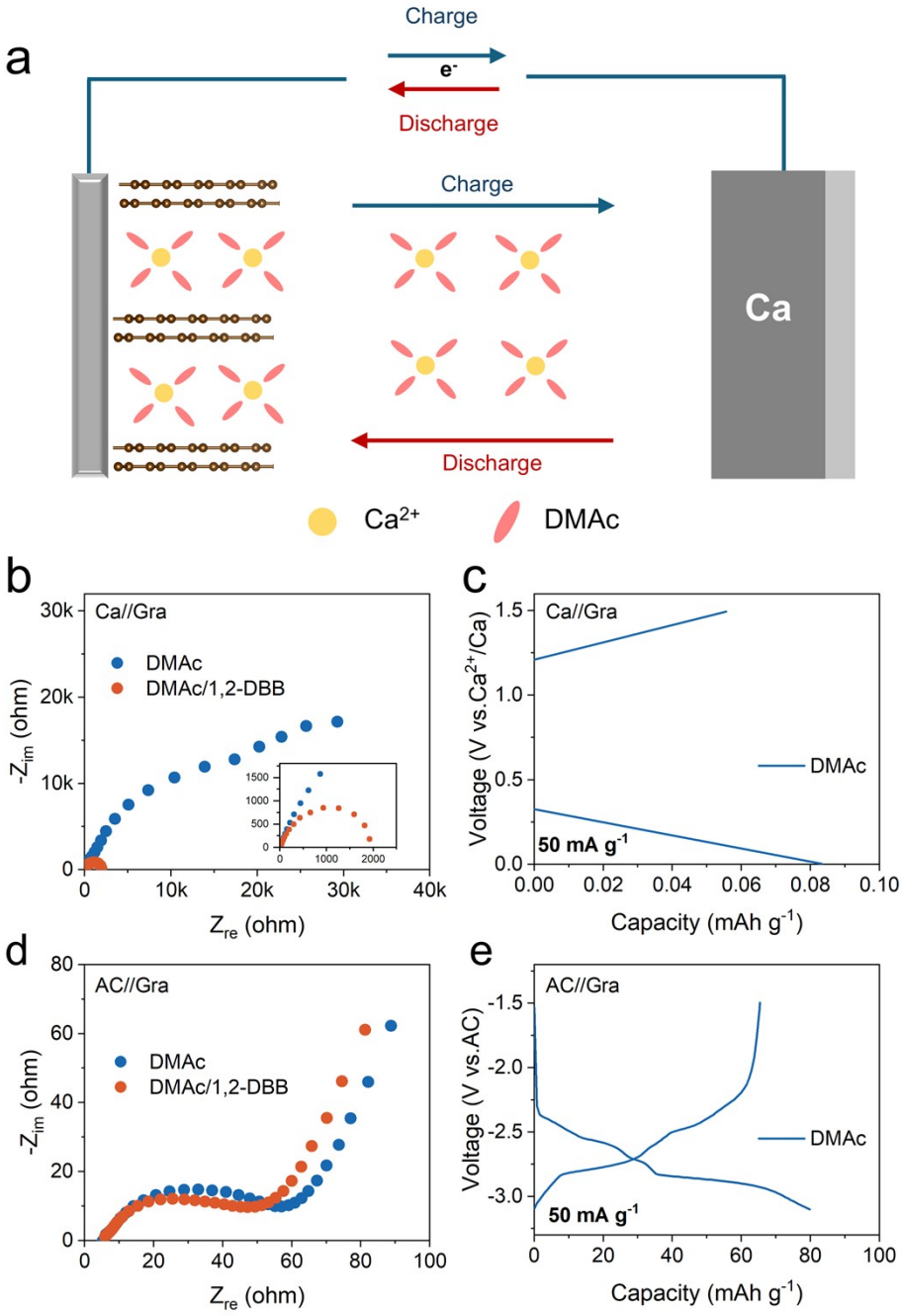

Figure S40. (a) Schematic illustration of working mechanism of Ca//Gra cells. (b) Nyquist plots of Ca//Gra cells in the DMAc and DMAc/1,2-DBB electrolytes. (c) Charge-discharge curves of the Ca//Gra cell in the DMAc electrolyte. (d) Nyquist plots of AC//Gra cells in the DMAc and DMAc/1,2-DBB electrolytes. (e) Charge-discharge curves of the AC//Gra cell in the DMAc electrolyte. The weak Van der Waals force among graphene layers provides sufficient space to accommodate solvated Ca^{2+} complexes, enabling insertion of Ca ions into graphite. The severe passivation of Ca metal in DMAc electrolyte causes high interfacial resistance and negligible capacity of Ca//Gra cells.

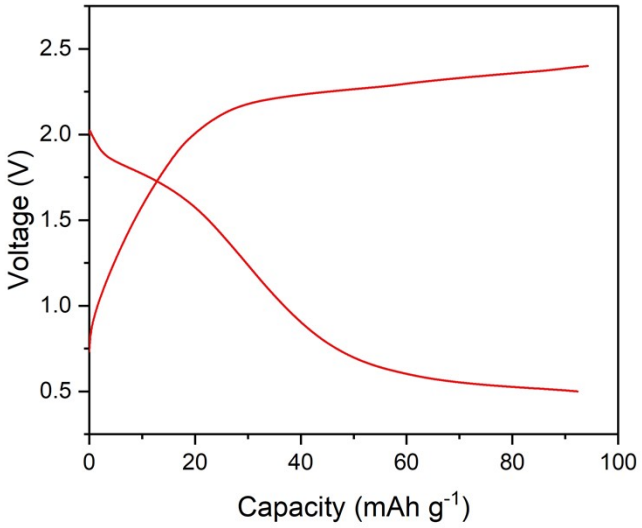

Figure S41. Charge-discharge curves of the Ca//PQ full cell in the DMAc/1,2-DBB electrolyte.

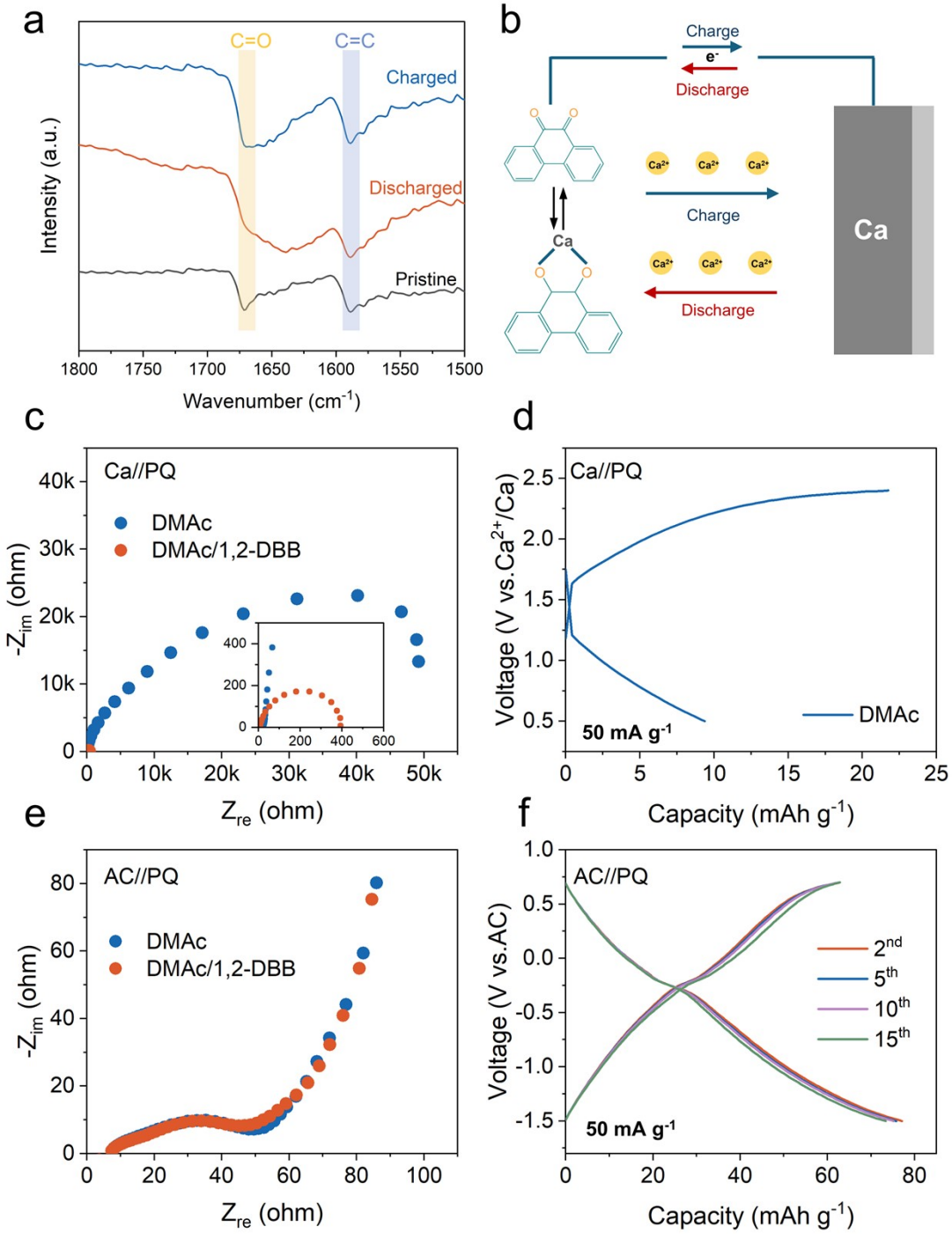

Figure S42. (a) FTIR spectra of pristine, discharged and charged PQ cathodes. (b) Working process of a Ca//PQ full cell. (c) Nyquist plots of Ca//PQ full cells in the DMAc and DMAc/1,2-DBB electrolytes. (d) Charge-discharge curves of the Ca//PQ cell in DMAc electrolyte. (e) Nyquist plots of AC//PQ cells in the DMAc and DMAc/1,2-DBB electrolytes. (f) Charge-discharge curves of AC//PQ cells in the DMAc electrolyte. The reversible (de)enolization of C=O motifs contribute to Ca^{2+} storage in PQ cathodes. Comparison of AC//PQ and Ca//PQ cells in DMAc electrolyte reveals that the failure of Ca//PQ is caused by unstable Ca metal anode rather than PQ cathode.

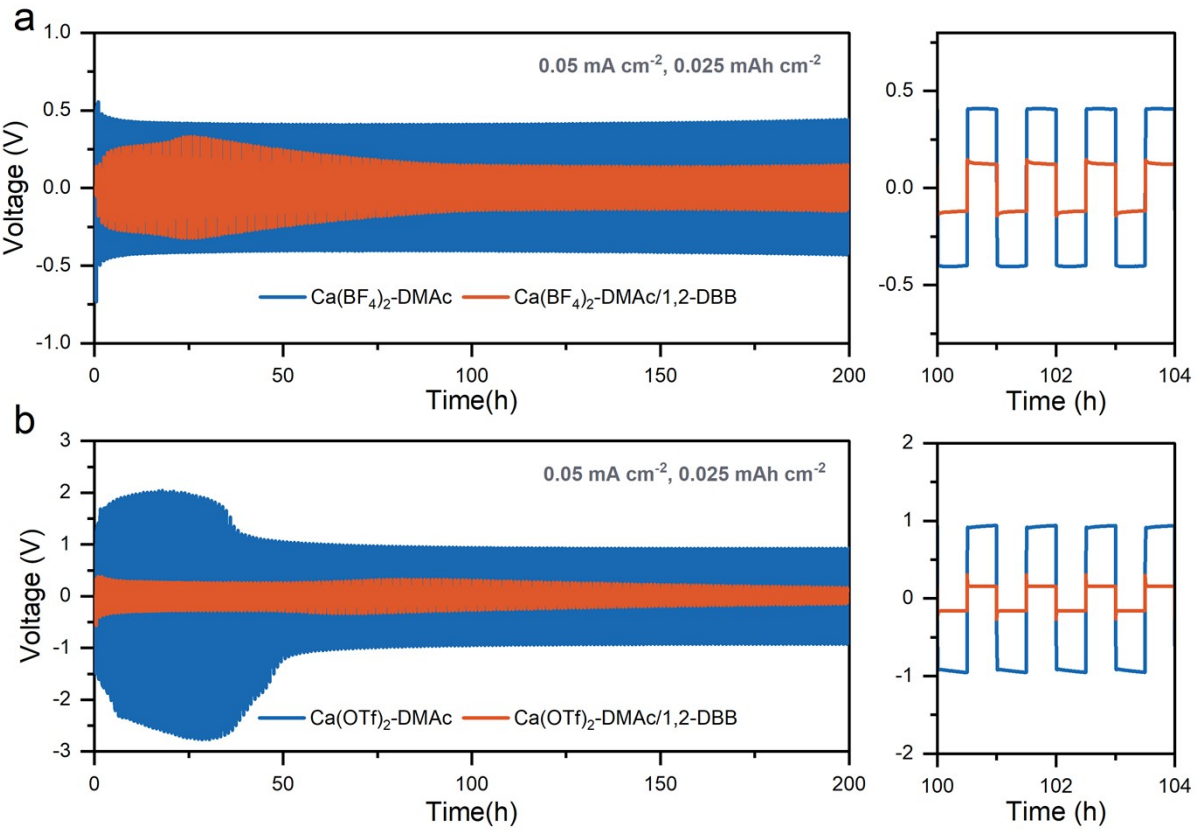

Figure S43. Cycling performance of Ca//Ca symmetric cells in (a) 0.3 M $Ca(BF_4)_2$ and (b) $Ca(OTf)_2$-DMAc electrolytes with and without 0.5 vol% 1,2-DBB additive at 0.05 mA cm^{-2} and 0.025 mAh cm^{-2}. The significantly decreased overpotentials for electrolytes with 1,2-DBB demonstrate the high versatility of anion-decoupling strategy across fluorinated Ca salts.

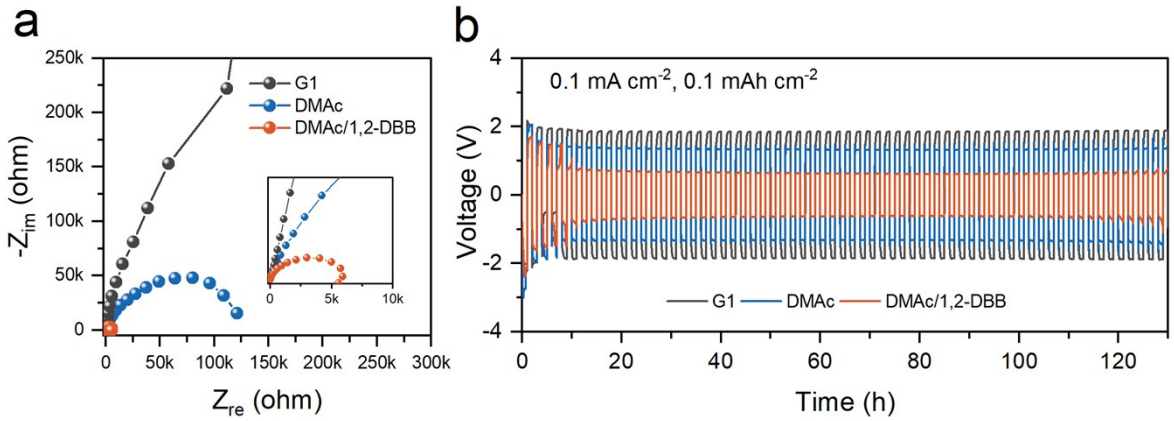

Figure S44. (a) Nyquist plots and (b) Cycling performance of Mg//Mg symmetric in 0.3 M $Mg(TFSI)_2$ G1, DMAc, and DMAc/1,2-DBB electrolyte solutions. Evidently, both interfacial impedances and the electrochemical overpotentials for Mg electrodes decrease in the order of G1 < DMAc < DMAc/1,2-DBB, demonstrating the applicability of our anion-decoupling mechanism in optimizing the interfacial kinetics for divalent metal anodes.

Table S1. Comparison of the electrochemical performance for Ca//Ca symmetric cells in peer electrolytes.

Electrolyte formulas	**Current density (mA cm^{-2})**	**Overpotential (V)**	**Cycle life (h)**	**References**
0.1 M $Ca(TFSI)_2$-DMAc	0.02	0.5	100	***Angew. Chem. Int. Ed.***, 2022, 134(50): e202214796
0.09 M $Ca(TFSI)_2$+1.71 M $LiBF_4$-FEC/G1	0.02	0.9	350	***Energy Environ. Sci.***, 2025, 18(4), 1941-1951
0.015 M CaI_2-G1/THFB	0.05	0.7	100	***Angew. Chem. Int. Ed.***, 2025, 64(1): e202413416
0.3 M $Ca(OTf)_2$-TMP/NMA	0.02	0.5	240	***ACS Materials Lett.***, 2025, 7, 3235−3242
0.1 M $Ca(TFSI)_2$-G1 ($Ca[B(hfip)_4]_2$	0.05	1.5	10	***Energy Environ. Sci.***, 2024, 17(18): 6548-6558
0.3 M $Ca(TFSI)_2$-DMAc/1,2-DBB	0.05	0.19	340	**This work**

References

[1] T. Lu, Q. Chen, *Chemistry–Methods* **2021**, *1*, 231-239.

[2] T. Lu, F. Chen, *J. Comput. Chem.* **2012**, *33*, 580-592.

[3] T. Lu, *J. Chem. Phys.* **2024**, *161*.